INVESTIGATING THE ROLE OF CALCIUM ON CORONAVIRUS MEMBRANE FUSION

A Thesis

Presented to the Faculty of the Graduate School

of Cornell University

In Partial Fulfillment of the Requirements for the Degree of

Master of Science

by

Miya Kristine Rubio Bidon

May 2022

ABSTRACT

Coronaviruses (CoVs) are a diverse family of enveloped viruses responsible for causing respiratory and/or enteric diseases across a wide range of species. The expansive animal host range of CoVs can be attributed to their ability to adapt to diverse cellular environments (*i.e.* pH, ions, proteases, receptors), and exploit different entry pathways to mediate viral-host cell membrane fusion and infect cells. Ions have arisen as an important factor in the viral membrane fusion mechanism. Within the CoV family, our team has found that calcium availability leads to increased virus infection of cells. Previously, we observed that calcium availability also promotes insertion of SARS FP into the host cell bilayer and subsequent membrane lipid ordering, pointing to the possible role of calcium in interacting directly with the FP during CoV membrane fusion activity. Due to the highly conserved nature of the FP within the CoV family, we chose to investigate the specific binding pockets of Ca^{2+} within SARS- and MERS-CoV. We used site-directed mutagenesis and infectivity assays to pinpoint specific residues that lead to changes in infectivity when calcium is present or not. We identified potential calcium-binding residues by substituting the charged residues (*i.e.* aspartic acid, glutamic acid) in the FP with non-charged amino residue, alanine. We compared the infectivity of mutant and wild-typed CoV pseudoparticles under calcium-rich or poor environments using available FDA-approved calcium blocking drugs. Our data suggests very similar residue coordination between SARS-CoV and SARS-CoV-2 as both FPs binds to two Ca^{2+}. Overall, these results demonstrate that Ca^{2+} have specific interactions

with the CoV FP and opens the possibility of utilizing FDA-approved calcium blocking drugs as a potential treatment against COVID-19.

BIOGRAPHICAL SKETCH

Miya Kristine Rubio Bidon was born in Quezon City, Philippines to Rosanna Bidon and Paul Bidon on December 28th, 1996. She received her B.S. in Chemical Engineering with a minor in Biochemistry from Worcester Polytechnic Institute in May 2018. She went on to pursue a PhD degree at the Robert Frederick Smith School of Chemical & Biomolecular Engineering at Cornell University in August 2018 and joined Professor Susan Daniel's research group in October 2018.

I dedicate this thesis to my family, friends, and all members of the Cornell community that supported me for the past few years.

ACKNOWLEDGEMENTS

First and foremost, I would like to thank my advisor, Dr. Susan Daniel, and my special committee members, Dr. Gary Whittaker and Dr. Hector Aguilar-Carreño. I thank all the past and present members of the Daniel Research Group for their continuous support and friendship, especially my mentor Dr. Tiffany Tang. I would like to thank Dr. Whittaker and the Whittaker lab, especially Dr. Marco R. Straus and Dr. Javier A. Jaimes for their guidance and mentorship, and Wendy Wingate for her unwavering support. I thank Dr. Harel Weinstein and Dr. George Khelashvili from Weill Cornell for teaching me about molecular dynamics simulations to better understand protein function. Lastly, I thank my friends, family, and my dog, Koda, for always being there for me during this chapter of my life.

TABLE OF CONTENTS

TABLE OF FIGURES

CHAPTER 1
INTRODUCTION

1.1. BACKGROUND

Coronaviruses (CoVs) are a diverse family of enveloped viruses responsible for causing respiratory and/or enteric diseases across a wide range of species [1]. It is imperative to understand CoV viral entry as more transmissible variants of SARS-CoV-2/COVID-19 arise for the development of alterative therapeutics as it has infected approximately more 200 million people worldwide and is responsible for more than 4 million deaths with more than 4 billion vaccine doses administered. Such knowledge is essential for the development of therapeutic treatments to counteract infection by these viruses.

The expansive animal host range of CoVs can be attributed to their ability to adapt to diverse cellular platforms (*i.e.* pH, ions, proteases, receptors), and exploit different entry pathways to mediate viral-host cell membrane fusion and infect cells [1]. Upon infection, CoV binds to their host cell receptor and the spike (S) protein, which dictates viral entry exposing the fusion peptide (FP) during a conformational change that fuses the host cell and viral membranes together [1]. Ions have arisen as an important factor in the viral membrane fusion mechanism. For instance, rubella virus is the first virus to require a calcium ion bridge within its FP to carry out successful membrane fusion, and ultimately viral infection to occur [2]. Recently a similar role for calcium in Ebolavirus infection was also discovered [3]. As such, recent reviews have suggested looking towards calcium channel blockers to repurpose these FDA-approved drugs against infection by these viruses [4, 5]. Given that CoVs show this sensitivity to calcium as

well, this strategy could be particularly useful against COVID-19 infection; however, calcium's method of action on viral fusion must be better understood first.

Within the CoV family, our team has found that calcium availability leads to increased viral infection of cells. Separately we observed that calcium availability promotes insertion of SARS FP into host cell bilayer and subsequent membrane lipid ordering, pointing to the possible of calcium in interacting directly with the FP during CoV membrane fusion activity [6]. As such, I hypothesize that this highly conserved fusion peptide is the target of calcium interaction, ultimately leading to changes in the functional outcome of the S protein that leads to higher infection by modifying the membrane fusion process.

In this chapter, background information regarding the CoV spike protein and the viral entry pathways will be provided. The role Ca^{2+} plays in the viral life cycle to hijack the cellular environment to ultimately benefit viruses will be discussed. This Ca^{2+}-virus interplay motivated this project to further uncover the calcium-dependent nature of CoV infection using functional and structural characterization of the fusion peptide.

1.2. CORONAVIRUS SPIKE PROTEIN

As was previously alluded, the CoV S protein has an important role in infection as it regulates viral entry into host cells. The S protein is one of the 4 structural proteins encoded by the CoV single-stranded, positive-sense RNA genome. In the viral membrane, the S protein participates in two events: receptor binding, and membrane fusion between viral and host cell membranes. These sequential events will trigger the

release of the viral RNA genome into the host cell, thus starting the viral replication cycle [7].

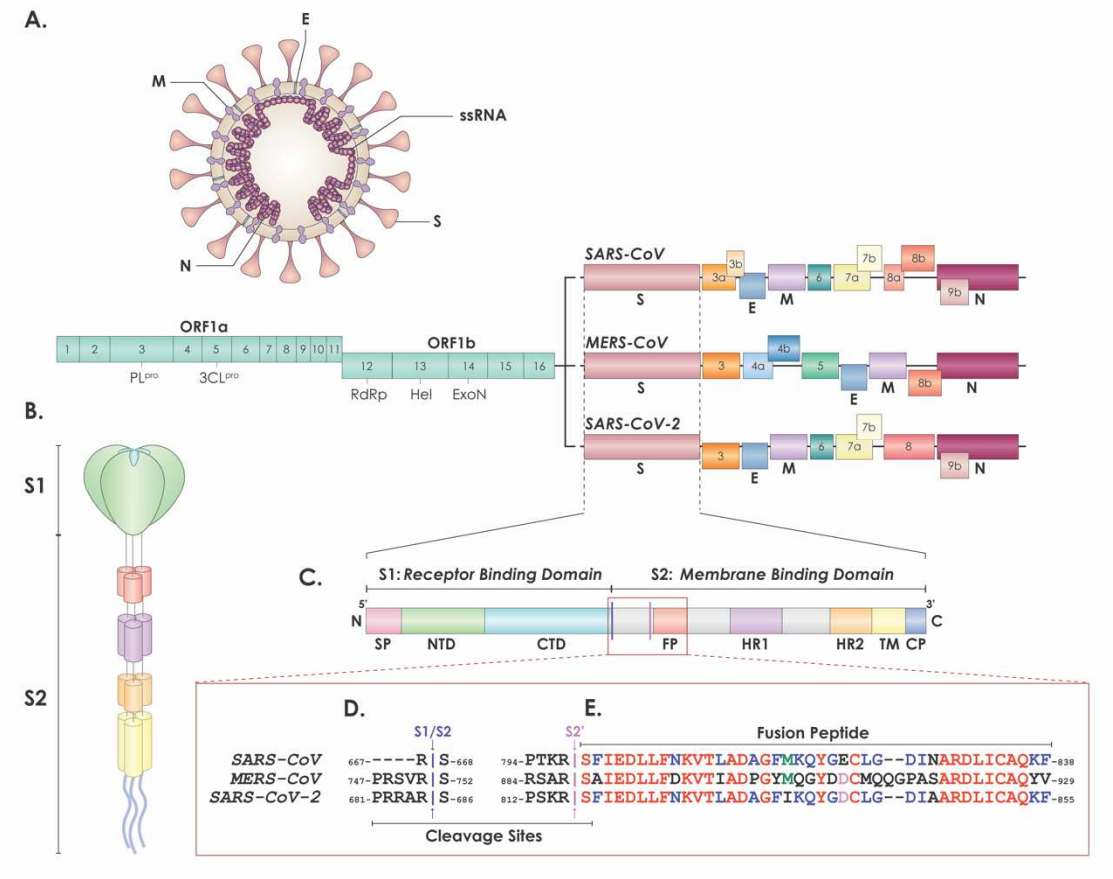

Figure 1. Coronavirus spike (S) protein. A. Cartoon figure of the CoV particle (top) and complete CoV viral genome (bottom). CoVs have a lipid envelope with three structural transmembrane proteins: spike (S), membrane (M), and envelope (E). The virus interior contains the viral genome encapsulated by the nucleocapsid (N) protein. The CoV single-stranded genome encodes for 16 nonstructural proteins, including the papain-like protease (PLpro), 3C-like protease (3CLpro), RNA-dependent RNA polymerase (RdRp), helicase (Hel), and exonuclease (ExoN). The subgenomic RNAs encode four structural proteins: spike (S, dark pink), envelope (E, envelope, dark blue), membrane (M, purple), and nucleocapsid (N, magenta), and a number of accessory proteins. B. Cartoon figure of the CoV S protein trimer. C. The CoV S gene denoting the functional components of the protein. The CoV S protein is composed of the two subunits: S1 and S2, encompassing the major functional components: SP (signal peptide, pink), NTD (N-terminal domain, green), CTD (C-terminal domain, light blue), FP (fusion peptide, red), HR1 (heptad repeat 1, purple), HR2 (heptad repeat 2, orange), TM (transmembrane, yellow), and CP

(cytoplasmic tail, dark blue). The S protein has two cleavage sites denoted with dark purple (S1/S2) and pink (S2') arrows. D. Sequence alignment of S1/S2 cleavage site (dark purple arrow) and S2' cleavage site (pink) between MERS-CoV, SARS-CoV, and SARS-CoV-2. E. Within the genome, the fusion peptide is highlighted, denoting the sequences from SARS-CoV, MERS-CoV, and SARS-CoV-2 FP. Red denotes the conserved residues between MERS-CoV, SARS-CoV, and SARS-CoV-2 FP sequences; blue denotes the SARS-CoV and SARS-CoV-2 FP conserved residues; green denotes the SARS-CoV and MERS-CoV FP conserved residues; purple denotes the MERS-CoV and SARS-CoV-2 conserved residues. The fusion peptide sequences of SARS-CoV-2 was determined by performing a pairwise alignment with MUSCLE through Geneious (version 2020.0.5). Amino acid sequence of the S proteins was obtained from NCBI Genbank based on the following: SARS-CoV-2 (MN908947.3), MERS-CoV (AFS88936.1), SARS-CoV (AAP1344.1).

Following viral release into the host cell, translation of the ORF produces 16 non-structural proteins forming the viral replicase-transcriptase complex. This complex aids in viral genome replication and subgenomic transcription encoding four structural proteins, spike (S), envelope (E), membrane (M), and nucleocapsid (N), along with several accessory proteins [8, 9]. Structurally, the S protein monomer is a ~180-200 kDa type I transmembrane protein, with the N-terminus facing the extracellular space, held in the viral membrane via its transmembrane domain, with a short C-terminal segment facing the intracellular space. The extracellular domain is split into two subunits, S1 and S2, which mediate receptor binding and membrane fusion, respectively. In its trimeric form, S protein form a crown-like halo surrounding the coronavirus S protein [10, 11]. Structural modeling of coronavirus S protein monomers show that S1 and S2 subunit form the bulbous head and stalk region, respectively.

The S1 subunit contains two subdomains: the N-terminal domain (NTD) and the C-terminal domain (CTD). One or both subdomains can serve as the receptor-binding domain (RBD) with the piece of the RBD directly contacts the receptor, also known as receptor binding motif (RBM). Both SARS-CoV and SARS-CoV-2 utilize the CTD to

bind angiotensin-converting enzyme 2 (ACE2), commonly detected on lung and small intestine cells. The RBM between SARS-CoV and SARS-CoV-2 show 50% sequence homology, which has been hypothesized to strengthen or weaken RBM-ACE2 associations, however, further experiments should be conducted to determine impact of these mutations on ACE2 binding [12, 13].

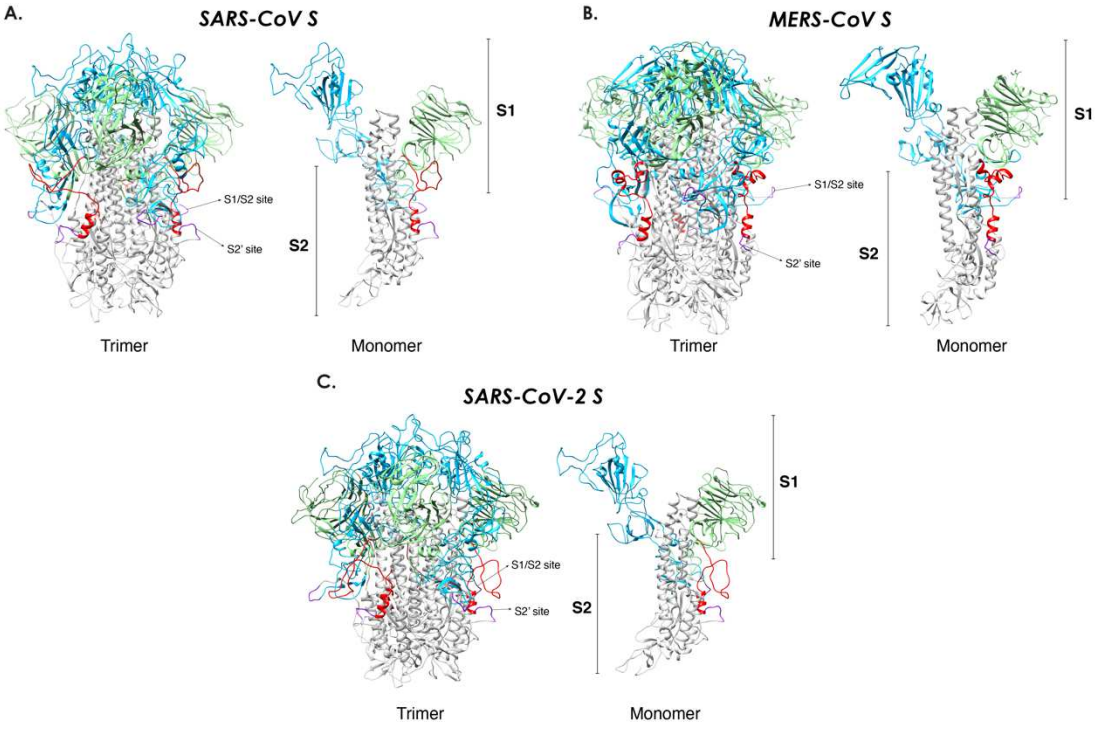

Figure 2. MERS-CoV (*A*), SARS-CoV (*B*), and SARS-CoV-2 (*C*) S protein models. Models were built to show the predicted structure of the S1/S2, the S2' cleavage site, and the FP, which are not solved in cryo-EM structures. Trimers and monomers were modeled using SARS-CoV (PDB 5X58) and MERS-CoV (PDB 6Q05) structures using the methodology described in Jaimes et al. Color scheme is as described in Fig 1.

The CoV S protein is also classified as a class I viral fusion protein, based on the structure of its fusion subunit [14]. This is largely composed of α-helical secondary structures, with its function regulated through proteolytic priming or cleavage at specific sites to induce the fusion-competent state of the S protein. The S2 or fusion subunit

contains a variety of motifs, notably the fusion peptide (FP), the functional fusogenic element of the S protein.

For SARS-CoV, several regions have been suggested as the FP. Using the Wimley and White interfacial hydrophobicity scale to identify regions with a higher propensity to insert into membranes, the peptide encompassing region 770-788 was shown to induce fusion and membrane leakage in large unilamellar vesicles. Separately, the region 798-835 was also identified as a fusion peptide as single point mutagenesis studies demonstrated its importance in fusion, containing a highly conserved region, SFIEDLLFNKV (798-808) [10]. An excellent review by Millet and Whittaker discusses the journey of identifying the SARS-CoV FP and its key findings. Based on the current understanding of the SARS-CoV FP, we suggest here a preliminary SARS-CoV-2 using a pairwise sequence alignment demonstrating strong conservation of 93% sequence similarity with SARS-CoV FP.

1.3. VIRAL ENTRY PATHWAYS

As discussed, CoV S mediates receptor binding and membrane fusion. However, two proteolytic cleavage events need to occur prior to membrane fusion. S protein needs to be primed by a protease at the S1/S2 interface and triggered immediately upstream of the FP (S2') [10, 11]. What makes CoV a versatile virus is its ability to adapt to different cellular environments and hijack different available proteases for infectivity. SARS-CoV, MERS-CoV, and SARS-CoV-2 can be triggered to fuse either at the plasma membrane or endosomal membrane, depending on protease availability.

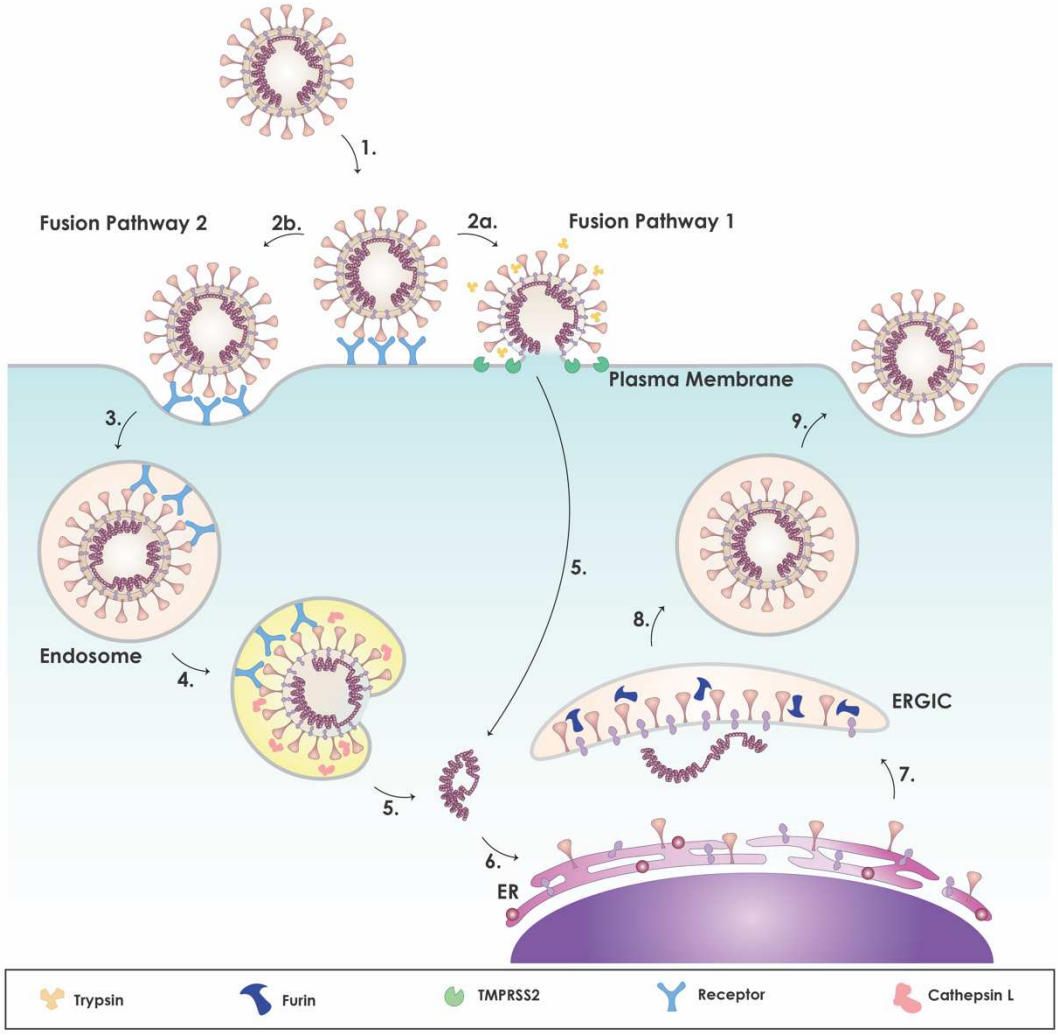

Figure 3. Model of coronavirus dual entry pathway. This model depicts the two methods of viral entry: early pathway and late pathway. As the virus binds to its receptor (*1*), it can achieve entry via two routes: plasma membrane or endosome. For SARS-CoV: The presence of exogeneous and membrane bound proteases, such as trypsin and TMPRSS2, triggers the early fusion pathway (*2a*). Otherwise, it will be endocytosed (*2b*, *3*). For MERS-CoV and SARS-CoV-2: If furin cleaved the S protein at S1/S2 during biosynthesis, exogeneous and membrane bound proteases, such as trypsin and TMPRSS2, will trigger early entry (*2a*). Otherwise, it will be cleaved at the S1/S2 site (*2b*) causing the virus to be endocytosed. For all three: Within the endosome, the low pH activates cathepsin L (*4*), cleaving the S2' site, triggering the fusion pathway and releasing the CoV genome. Upon viral entry, copies of the genome are made in the cytoplasm (*5*), where components of the spike protein are synthesized in the rough endoplasmic reticulum (ER) (*6*). The structural proteins are assembled in the ER-Golgi intermediate compartment (ERGIC), where the spike protein can

be pre-cleaved by furin, depending on cell type (*7*), followed by release of the virus from the cell (*8*, *9*).

1.3.1. EARLY PATHWAY: PLASMA MEMBRANE ROUTE

Trypsin was found to induce cell-cell fusion in SARS-CoV, MERS-CoV, and SARS-CoV-2. In fact, with trypsin, the sequential cleavage steps were able to be determined. Studies found trypsin treatment following pseudoparticle binding resulted in effective infection at the plasma membrane route, whereas trypsin treatment prior to binding is hypothesized to invoke irreversible conformation changes to S that inhibits its fusion function [15-17].

In addition to exogeneous proteases, transmembrane proteases, such as type II transmembrane serine proteases (TTSPs), were found to activate, and enable viral spread, such as in the case of influenza. TTSP-activated CoV entry was investigated where it was determined that cells expressing TMPRSS2 supported SARSpp and live SARS-CoV infection at the plasma membrane route without exogeneous or endosomal proteases [18, 19]. This behavior is also found to activate MERS-CoV and SARS-CoV-2 infection [20, 21].

Although there is a high degree of sequence conservation between SARS-CoV, MERS-CoV, and SARS-CoV-2 S2 membrane fusion domains, there are key differences in the fusion membrane for plasma membrane entry. For instance, SARS-CoV-2 possesses a unique insert by the S1/S2 site that can be processed by furin, unique for SARS-like CoVs [22]. Western blots have shown S proteins in SARS2pp to be processed at the S1/S2 site during biosynthesis in a similar fashion to MERS-CoV. However, studies by Tang *et al* found that other proprotease convertase (PCs) may also be involved in activating the S1/S2 loop as they found poor processing of uncleaved S

upon the addition of purified furin and limited impact of infectivity when using a highly selective furin inhibitor (alpha1-PDX) [23]. SARS-CoV S, in comparison, is not cleaved during biosynthesis and does not require a S1/S2 pre-cleavage event for plasma membrane fusion. It has been observed that SARS-CoV S binds its receptor with a 10- to 20- fold higher affinity compared to MERS-CoV S with its receptor, so strong receptor binding may better support SARS-CoV plasma membrane entry [15].

1.3.2. LATE PATHWAY: ENDOSOMAL ROUTE

In the absence of exogeneous or membrane-bound proteases that enable entry at the plasma membrane surface, CoVs can be internalized via clatherin- and non-clatherin-mediated endocytosis [24]. As the virus is shuttled along the endocytic pathway towards the cell interior, the endosomal pH decreases. For some viruses (*i.e.* influenza, vesicular stomatitis virus), low pH triggers fusion, however in the case of SARS-CoV, low pH exposure to SARSpp did not reduce infectivity, suggesting that other factors may be playing a role in CoV endosomal fusion [10, 14].

The low pH environment also activates endosomal protease, such as cathepsins, a family of cysteine proteases, specifically cathepsin B and L which respectively activate in the early and late endosome. Subsequent studies were performed on MERS, SARS, and SARS-CoV-2 pseudoparticles to distinguish which cathepsin is involved in membrane fusion [10, 14, 25]. From that, it is believed the CoVs (MERS, SARS, and SARS-2) are indirectly dependent on low pH as it is necessary to activate cathepsin L protease, thereby cleaving the S2' site to catalyze the subsequent fusion steps.

1.4. MEMBRANE FUSION

Viral membrane fusion is the process by which enveloped viruses merge their membrane with the host cell membrane to deliver the viral genome into the cell, resulting the production of new virions. CoV membrane fusion occurs after receptor binding, requiring the viral fusion protein to catalyze this reaction by providing high energy required to bring the membranes closer together [10, 14].

As previously mentioned, CoV S protein is a class I fusion protein. As such they catalyze the membrane fusion reaction through the following sequential states: (1) pre-fusion native state, (2) pre-fusion metastable state, (3) pre-hairpin intermediate state, (4) post-fusion stable state [10, 14]. S protein synthesis adopts a pre-fusion native state which in turn transition into a pre-fusion metastable state upon S1/S2 cleavage, thus non-covalently separating S1/S2 domains [10, 14].

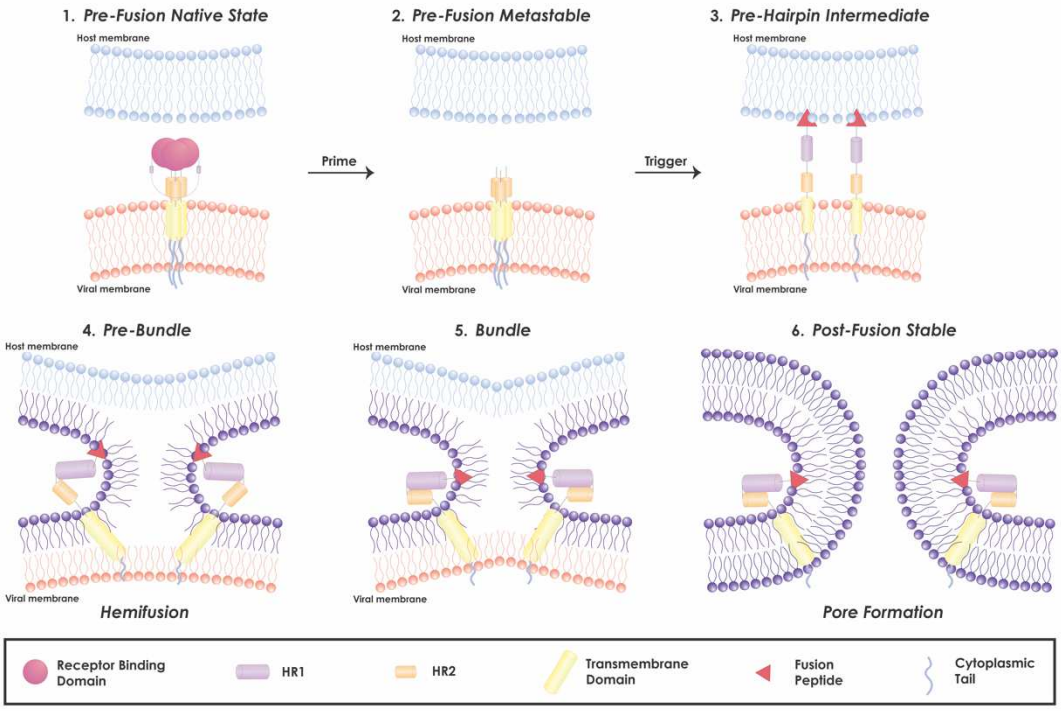

Figure 4. Coronavirus viral fusion pathway model based on class I fusion protein understanding. The captions above the figure describe the state of the fusion peptide, the captions below describe the state of the membranes. The S protein starts in the pre-fusion native state (*1*) and undergoes priming of the S1 subunit by relevant proteases to achieve the pre-fusion metastable state (*2*). Subsequent triggering by relevant proteases will enable the FP to insert in the host membrane and allow the S protein to form the pre-hairpin intermediate (*3*). The pre-hairpin begins to fold back on itself due to HR1 and HR2 interactions forming the pre-bundle (*4*), bundle (*5*), and eventual post-fusion stable (*6*) states. During the S protein foldback, the two membranes will approach each other until the outer leaflets merge (*hemifusion*) and eventually the inner leaflets merge (*pore formation*).

In the metastable state, the fusion protein must be exposed to a trigger to induce a series of conformational changes to enable FP membrane insertion, forming a pre-hairpin intermediate state. After insertion the three HR1 regions and HR2 regions will assemble to form a fusion core, or six-helix bundle, that pulls the viral and host cell membrane to proximity to fuse [10, 14]. This process of membrane fusion is composed of two stages: hemifusion and pore formation. Hemisfusion is defined as the outer leaflets from each opposing membrane will merge but no other content mixes [10, 14]. Pore formation will follow soon after, forming a connection between the viral interior and host cell cytoplasm, allowing the virus to release its genetic material through the pore [10, 14].

1.5. ROLE OF IONS IN MEMBRANE FUSION

Calcium ions, one of the most evolutionarily universal and versatile signaling molecules, are involved in almost all functional aspects of life. This diverse versatility in Ca^{2+} signaling allows the modulation of many signaling components, namely ion channels, pumps, and receptors. As calcium is a vital aspect in many cellular processes, it is also a key component to enable viruses to hijack the host cell machinery and

proliferate in two major ways, disruption of Ca^{2+} homeostasis or Ca^{2+} binding to viral proteins [26].

Ca^{2+} has many functions with the viral proteins, specifically to maintain the structural integrity and/or assisting in the assembly and disassembly of virions. Initial studies discovered the rubella virus fusion machinery to specifically coordinate with Ca^{2+} for proper orientation and insertion into the host membrane [2]. Later, it was shown that Ebolavirus fusion machinery to also coordinate with Ca^{2+}.[3] These studies prompted closer investigation on the impact Ca^{2+} may have on SARS-CoV and MERS-CoV infectivity. By treating with extracellular and/or intracellular calcium chelating compounds, it is possible to determine changes in infectivity under Ca^{2+} depleted conditions. Studies from Lai *et al* and Straus *et al* demonstrated calcium dependence for both SARS-CoV and MERS-CoV in the endocytic route when intracellular calcium was chelated in VeroE6 and Huh7, respectively. Ca^{2+} interaction was further examined using biophysical techniques [6, 27]. With electron spin resonance (ESR), SARS, SARS-2 and MERS FPs were found to undergo greater membrane ordering under the presence of calcium, indicating Ca^{2+} may stabilize the FP structure to promote fusion. Isothermal calorimetry experiments demonstrated the SARS-CoV-2 to specifically bind to Ca^{2+} compared to other ions that may be present in the cellular environment (*i.e.* Mg^{2+}, K^{+}, Na^{+}) [28] and highlighted differences in Ca^{2+}-FP binding as MERS-CoV FP binds to one Ca^{2+} ion, whereas SARS-CoV and SARS-CoV-2 FPs binds two [6, 27, 28]. Mutagenesis experiments conducted on MERS-CoV FP identified one negatively charged amino acid, E891, in the FP1 domain to bind to Ca^{2+} while molecular dynamic simulations predicted the two Ca^{2+} ions to bind to E819/D820 and D830/D839 to

mediate the most optimal conformational state of the FP for the maximal membrane penetration [29]. Further studies on SARS-CoV investigating their Ca^{2+} binding sites should be performed, which will not only further demonstrate the Ca^{2+} dependent nature of the CoV FP but also potential conservation of binding pairs among the Coronaviridae family.

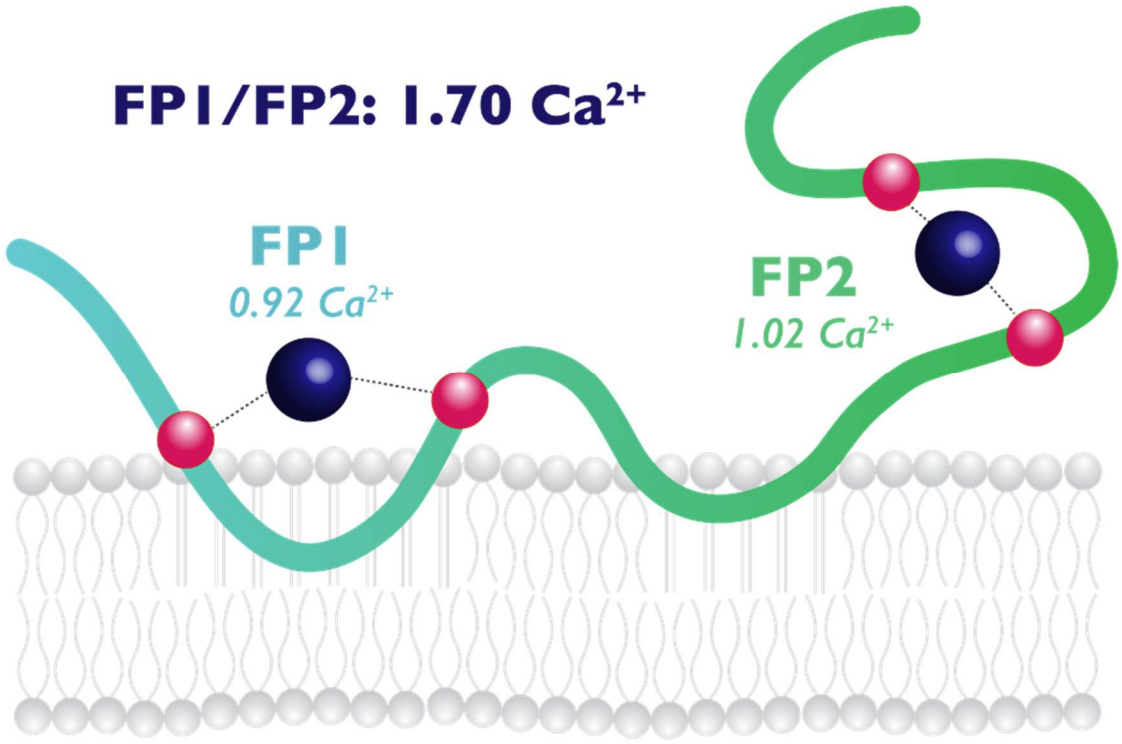

Figure 5. Proposed model of the CoV FP platform with the lipid bilayer under the presence of Ca^{2+}. This model previously proposed by Lai *et al* 2017 depicts the key features of the FP: its bipartite nature and calcium binding ability to two Ca^{2+} ions during membrane fusion.

CHAPTER 2
THE INTERACTIONS OF CALCIUM IONS WITH SPECIFIC RESIDUES IN THE SARS-COV FUSION PEPTIDE AND THE REGULATION OF VIRAL INFECTIVITY

2.1. INTRODUCTION

Coronaviruses (CoVs) are a diverse family of enveloped, positive-sense, single-stranded RNA viruses responsible for causing respiratory and enteric diseases across a wide range of species [30, 31]. Three pathogenic human coronaviruses have emerged during the early 21st century: in 2002, severe acute respiratory syndrome (SARS-CoV) [32]; in 2012, Middle East respiratory syndrome (MERS-CoV) [33]; and presently, SARS-CoV-2 [13, 34]. The World Health Organization has listed coronaviruses in the top five emerging pathogens likely to cause major epidemics, in part, because minimal countermeasures exist [35-37]. While vaccines are one strategy that has proven to be successful during this SARS-CoV-2 pandemic, there is an outstanding need for antiviral drugs as a necessary parallel line of defense. To develop antiviral interventions, it is necessary to understand the fundamental biology of the virus and its host interactions, with interventions ideally targeting a well-conserved part of the virus life cycle to confer the broadest protection. Viral entry is indeed a conserved function [1, 38], with the coronavirus spike (S) protein controlling virus entry through its interaction with the host cell plasma membrane. Examining the entry functions of the S protein can point to vulnerable targets that can be exploited for drug intervention.

The CoV S protein is composed of two subunits, S1 and S2, that responsible for facilitating receptor binding and membrane fusion, respectively [1, 11, 39]. An interesting characteristic of CoV entry is that the virus can enter the host cell using two different pathways: an "early" pathway, often referred to as a plasma membrane route, or a "late" pathway that follows an endosomal route [1]. The pathway used by the virus is dependent on the host cell type, and more specifically, on the local protease environment [40]. The current thinking is that SARS-CoV, MERS-CoV and SARS-CoV-2 take the early pathway when transmembrane-bound proteases (TTSPs) such as the TMPRSS2 are present, while in cell lines without TTSPs the virus follows an endosomal route where it interacts with lysosomal proteases (*i.e.* cathepsin L) [1, 10, 41]

This pathway flexibility arises from the requirement for protease cleavage to prime the S protein for subsequent conformation changes needed to carry out membrane fusion. There are two possible cleavage sites in the S protein: S1/S2 and S2' [14]. The first site is located at the boundary of the S1 and S2 domains and, when present, is typically cleaved by furin during virus assembly; it separates the binding domain from the fusion machinery. S2' is located next to the N-terminus of the conserved fusion peptide (FP) segment that is liberated upon cleavage [42]. S2' cleavage is a required event that allows the S2 domain to undergo a large conformational change that positions the FP for insertion into the host cell membrane [1]. FP insertion is a key step in commencing the process of merging the host cell membrane with the viral envelope that is necessary to transfer the viral genome into the host cell cytosol.

Given the importance of the FP in initiating membrane fusion, it is not surprising to find significant conservation of amino acid sequence in this region of S across many CoVs [6]. Returning to the strategy of identifying a well-conserved function for possible antiviral target, the FP stands out as an important prospect. Thus, much work by our team and others has focused on understanding the structure-function of the FP and has identified key residues of importance for interaction with calcium ions (Ca^{2+}) that lead to productive membrane interaction and successful infection [3, 6, 27-29].

In our previous studies, we showed that for both SARS-CoV and MERS-CoV, calcium depletion in cell culture leads to a significant drop in cell infection [6, 27]. We connected this observation with fusion, observing that syncytia formation during cell-to-cell fusion between S- and ACE2 receptor-expressing VeroE6 cells also drops in calcium-depleted media. We then sought to connect this observed impact on fusion with the molecular scale features of S that may interact directly with calcium ions. Within the S2 domain, the FP sequence has strong conservation of charged amino acids at specific positions flanking the hydrophobic residues that interact with the host membrane upon insertion [6]. We posited that these charged residues could function as sites for calcium ion binding that may stabilize the local structure of the FP and position it for optimal insertion. Through a series of biophysical and biochemical techniques, our group confirmed that indeed, calcium does interact directly with the FP and that this interaction can be linked to infection. Thus, we determined with isothermal calorimetry the stoichiometry of interaction between the FP and calcium ions to be two for SARS-CoV [6, 28] and one for MERS-CoV [27]. From circular dichroism (CD) measurements, we observed that in the presence of calcium and membranes, the FP adopts a

conformation with a higher degree of alpha helicity. From electron spin resonance spectroscopy (ESR) results we found lipid ordering upon FP insertion, which can contribute to membrane fusion, with more lipid ordering occurring in the presence of Ca^{2+} [6, 43]. Finally, in these earlier studies, we carried out selected point substitutions of amino acids in the FP, exchanging charged amino acids for alanine, and observed that infectivity dropped in some cases [42]. Recent findings show that calcium is necessary to promote viral entry across multiple coronaviruses, including SARS-CoV [6], MERS-CoV [27], and SARS-CoV-2 [28, 29]. More studies of the fusion peptide's membrane interactions have been carried out using nuclear magnetic resonance (NMR) [44].

Taken together, these results revealed the FP region of the S protein as the key domain for calcium interaction, and membrane insertion; increased infectivity, results from FP structural changes introduced by calcium ion binding. Despite these studies, the initial model for the interaction of calcium with the negatively charged residues of the SARS-CoV FP [6], still lacks a detailed structural understanding of how Ca^{2+} ions stabilize the FP for membrane insertion.

Here, we present specific mechanistic insight gathered from extensive mutagenesis studies and computational simulations of the FP and calcium. This work illuminates the relationship between the preferred modes of calcium binding to the acidic residues of the coronavirus FP and how those modes regulate membrane interactions and subsequent infectivity. We examined the effects of mutating individual charged residue in SARS-CoV FP, as well as key pairs and trios, to identify the residues involved in productive interactions with calcium ions. We then used corresponding molecular

dynamics simulations of the system to interpret these results structurally. From these simulations we identified the structures and probabilities of FP's modes of calcium binding in 1:1 and 2:1 stoichiometries and determined the structure of the SARS-CoV FP that is best suited for membrane interaction and penetration.

2.2. MATERIALS & METHODS

2.2.1. CELLS, PLASMIDS, AND REAGENTS

Human embryonic kidney 293 (HEK293T) and African green monkey kidney epithelial (VeroE6) cells were obtained from the American Type Culture Collection (ATCC, Manassas, VA). Both cell lines were grown in cDMEM, composed of Dulbecco's modified Eagle medium (DMEM, CellGro), supplemented with 10% HyClone FetalClone II (GE) and 25 mM HEPES (CellGro) at 37°C and 5% CO_2. Cells were passaged using 1X Dulbecco's Phosphate-Buffered Saline (DPBS) and Trypsin EDTA 1X (CellGro).

The plasmids used for generating pseudoparticles are: pCMV-MLV gag-pol murine leukemia virus (MLV) packaging construct, pTG-Luc transfer vector-encoding luciferase reporter, and pCAGGS-VSVG plasmid were produced as previously described [45]and provided by Jean Dubuisson (Lille Pasteur Institute, Lille, France). The C9-tagged SARS-CoV spike protein (pcDNA3.1-SARS-CoV S) was provided by Dr. Michael Farzan, New England Primate Research Center.

Recombinant L-1-tosylamide-2-phenylethyl chloromethyl ketone (TPCK)-treated trypsin was obtained from Sigma. Calcium chelator, EGTA, was obtained from VWR. The membrane-permeable, calcium-specific chelator, BAPTA-AM (acetoxymethyl ester) was obtained from Tocris and diluted in dimethyl sulfoxide (ThermoFisher).

2.2.2. SITE-DIRECTED MUTAGENESIS

Site-directed mutagenesis was performed on the SARS-CoV spike protein vector, pcDNA3.1-SARS-CoV-S via QuikChange Lightning site directed mutagenesis kit (Aligent). PCRs and transformations were performed based on the manufacturer's recommendations. Primers obtained from IDT Technologies were determined using the primer design tool from Aligent. The following primers were used to generate the SARS-CoV S mutants as listed in the table below:

Mutation	Forward Primer	Reverse Primer
E801A	GCGCAGCTTCATCGCGGACCTGCTCTTCA	TGAAGAGCAGGTCCGCGATGAAGCTGCGC
E801M	TGTTGAAGAGCAGGTCCATGATGAAGCTGCGCTTGG	CCAAGCGCAGCTTCATCATGGACCTGCTCTTCAACA
E801Q	GAAGAGCAGGTCCTGGATGAAGCTGCGCT	AGCGCAGCTTCATCCAGGACCTGCTCTTC
E801K	TTGAAGAGCAGGTCCTTGATGAAGCTGCGCTTG	CAAGCGCAGCTTCATCAAGGACCTGCTCTTCAA
E801D	GTTGAAGAGCAGGTCGTCGATGAAGCTGCGC	GCGCAGCTTCATCGACGACCTGCTCTTCAAC
D802A	CTTGTTGAAGAGCAGGGCCTCGATGAAGCTGCG	CGCAGCTTCATCGAGGCCCTGCTCTTCAACAAG
D812A	TGAAGCCGGCGGCGGCCAGCGTC	GACGCTGGCCGCCGCCGGCTTCA
E821A	CGCCCAGGCACGCGCCGTACTGC	GCAGTACGGCGCGTGCCTGGGCG
D825A	CGGGCGTTGATGGCGCCCAGGCACT	AGTGCCTGGGCGCCATCAACGCCCG
D830A	GCGCAGATCAGGGCGCGGGCGTTGA	TCAACGCCCGCGCCCTGATCTGCGC
E821A/D825A	CGGGCGTTGATGGCGCCCAGGCACG	CGTGCCTGGGCGCCATCAACGCCCG
E821A/D830A	GCGCAGATCAGGGCGCGGGCGTTGA	TCAACGCCCGCGCCCTGATCTGCGC
D825A/D830A	GCGCAGATCAGGGCGCGGGCGTTGA	TCAACGCCCGCGCCCTGATCTGCGC
E821A/D825A/D830A	GCGCAGATCAGGGCGCGGGCGTTGA	TCAACGCCCGCGCCCTGATCTGCGC

Mutations were confirmed via Sanger Sequencing at the Cornell University Life Sciences Core Laboratories Center.

2.2.3. WESTERN BLOTTING

8×10^5 HEK293T cells were seeded in poly-D-lysine coated 6-well plates and transfected WT or mutant SARS-CoV S protein-expressing pcDNA plasmid using polyethylenimine (PEI) (Fisher). To transfect each well, 2 µg DNA and 6 µL PEI were incubated with 50 µL OptiMEM (Gibco) for 20 minutes. After 20 minutes, 2 mL cDMEM was added to the transfection mix and then replaced the cell media. Cells were left to incubate in the transfection mix for 24 hours. For wells treated with TPCK-

trypsin, cells were washed once with 1X DBPS and 1 mL DPBS was supplemented with 0.8 nM TPCK-trypsin. Trypsin-treated cells incubated for 10 minutes at 37°C and 5% CO_2. The following analysis of spike protein cleavage: cell-surface biotinylation, western blotting, and antibody analysis were performed as previously described [7]. Briefly, SARS-CoV S protein was detected using the SARS-CoV S rabbit polyclonal antibody (NR-4569, BEI resources) as the primary antibody and Alexa Fluor 488-labeled goat anti-rabbit secondary antibody (Invitrogen). Western blots were visualized and analyzed using a Chemidoc system with Image Lab image capture software (BioRad). All bands have only been adjusted in contrast and brightness using the Image Lab software.

2.2.4. IMMUNOFLUORESCENCE ASSAY

3.5×10^5 VeroE6 cells were seeded in microscopy chamber slides (Millipore). After 24 hours, cells were transfected with a mixture containing 0.75 µL of Turbofect (Thermofisher), 0.5 µg S-expressing plasmid, and 11.75 µL OptiMEM for each well, and incubated for 24 hr. To activate S, cells were again washed with 1X DPBS and supplemented with 0.8 nM TPCK-trypsin for 5 minutes at 37°C and 5% CO_2. Cells were then fixed with 4% paraformaldehyde (PFA) (ThermoFisher) for 15 minutes and washed three times with DPBS. For the permeabilized condition, 0.1% Triton X-100 was added to each well for 5 minutes over ice and washed three times with DPBS. Cells were then blocked with 5% normal goat serum for 30 minutes and labeled with SARS-CoV S rabbit polyclonal antibody (NR-4569, BEI resources), followed by labeling with Alexa Fluor 488-labeled goat anti-rabbit secondary antibody (Invitrogen). The cell nuclei were labeled with DAPI (Southern Biotech). Microscopy images were acquired

using an upright microscope (Echo Revolve) with a 10x objective. To quantify the number of nuclei per syncytia, three randomly selected fields were acquired and manually counted. The average and standard deviation were calculated and visualized using Microsoft Excel and GraphPad Prism 7.

2.2.5. PSEUDOPARTICLE ASSAY

The production and infection of pseudoparticles (PPs) were performed as previously described [27, 45]. For pseudoparticle production, 3.5×10^5 HEK293T cells were seeded in 6 well plates. Pseudoparticles were prepared with 600 µg of their respective SARS WT and mutant S plasmids, 800 µg pTgG-luc, and 600 µg pCMV-MLVgagpol using polyethylenimine (PEI) as the transfection reagent. The cell supernatant was harvested 48 hours post-transfection, centrifuged at 1200 rpm for 7 minutes to separate from residual cellular debris, filtered through a 0.45 µm syringe filter, and stored at -80°C for one freeze-thaw cycle. For PP infectivity, 5×10^5 VeroE6 cells were seeded in 24 well plates and infected with PPs for 72 hrs at 37°C at 5% CO_2. Readings after PP infectivity were performed using a luminometer, Glomax 20/20 system (Promega). Each experiment contained three technical replicates and was repeated at least three times. Data analysis was performed using graphical software, GraphPad Prism 7.

For the calcium studies, calcium present in the extracellular and intracellular environments were chelated based on the methods previously described [27]. Briefly, to chelate extracellular calcium, VeroE6 were pre-treated with 200 µL DMEM- (Gibco; DMEM without L-glutamine, sodium pyruvate, HEPES, calcium; 2% HyClone; 10 mM HEPES) for 1 hour at 37°C and 5% CO_2. DMEM- pretreatment was aspirated after incubation and VeroE6 cells were subsequently treated with 200 µL PPs treated with 50

μM EGTA for 2 hours at 37°C and 5% CO_2 , and supplemented with 300 μL cDMEM post-incubation. VeroE6 cells pretreated with 200 μL DMEM+ (Gibco; DMEM without L-glutamine, sodium pyruvate, HEPES; 2% HyClone; 10 mM HEPES) and infected with untreated PPs serve as the negative control. To chelate intracellular calcium, VeroE6 cells were pretreated with 200 μL of 50 μM BAPTA-AM (dissolved in DMSO) in DMEM+ in the same conditions as described above. Cells were then infected with 200 μL PPs treated with 50 μM BAPTA-AM for 2 hours and supplemented with cDMEM post-incubation. VeroE6 cells pretreated with equivalent volumes of DMSO in 200 μL DMEM+ (Gibco; DMEM without L-glutamine, sodium pyruvate, HEPES; 2% HyClone; 10 mM HEPES) and infected with PPs treated with equivalent volumes of DMSO serve as the negative control for the intracellular calcium conditions. Analysis of infectivity under both extracellular and intracellular calcium chelation conditions were performed as described above.

To confirm the presence of the S protein in the PP, 1.5 mL of harvest PP was spun down using an ultracentrifuge in a TLA-55 rotor (Beckman-Coulter) at 42,000 × *g* for 2 hours at 4°C. The supernatant was aspirated, and the S protein pellet was resuspended in 2X Laemmli buffer and 1 M DTT. All protein was loaded on an SDS-PAGE gel, and Western blot analysis was performed as described above.

2.2.6. MODELING OF SARS-COV FUSION PEPTIDE

The structural cartoon model of the SARS-CoV S protein fusion peptide was based on the SARS-CoV S prefusion structure from the Protein Data Bank (PBD), PDB 5XLR. Protein alignments of the SARS-CoV S protein (GenBank accession no. AAT74874.1) with the respective SARS-CoV structure was performed with Geneious software

(v.2020.1.1). The structural models of the SARS-CoV was generated using the Modeller comparative modeling tool (v.9.23) within the Chimera software (v.1.13; University of California). Images were created using Adobe Illustrator CC v.24.03.

2.2.7. MOLECULAR DYNAMICS (MD) SIMULATIONS OF THE SARS-COV FP IN WATER

For all the atomistic MD simulations, the SARS-CoV FP segment was capped with neutral N- and C-termini (ACE and CT3, respectively, in the CHARMM force-field nomenclature). Protonation states of all the titratable residues were predicted at pH 7 using Propka 3.1 software [46].

For the simulations in water, one copy of the peptide (wild type or a mutant) was embedded in a rectangular solution box and ionized using VMD tools ("Add Solvation Box" and "Add Ions", respectively) [47]. The box of dimensions ~90 Å x 80 Å x 82 Å included a Na^+Cl^- ionic solution as well as 2 Ca^{2+} ions, and ~18000 water molecules. The total number of atoms in the system was ~54,540.

The system was equilibrated with NAMD version 2.13 [48] following a multi-step protocol during which the backbone atoms of the SARS-CoV FP as well as Ca^{2+} ions in the solution were first harmonically constrained and subsequently gradually released in four steps (totaling ~3ns), changing the restrain force constants k_F from 1, to 0.5, to 0.1 kcal/ (mol $Å^2$), and 0 kcal/ (mol $Å^2$). These simulations implemented all option for rigidbonds, 1fs (for k_F 1, 0.5, and 0.1 kcal/ (mol $Å^2$)) or 2fs (for k_F of 0) integration time-step, PME for electrostatics interactions [49], and were carried out in NPT ensemble under isotropic pressure coupling conditions, at a temperature of 310 K. The Nose-Hoover Langevin piston algorithm [50] was used to control the target P = 1 atm pressure

with the "LangevinPistonPeriod" set to 200 fs and "LangevinPistonDecay" set to 50 fs. The van der Waals interactions were calculated applying a cutoff distance of 12 Å and switching the potential from 10 Å.

After this initial equilibration phase, the velocities of all atoms in the system were reset and ensemble MD runs were initiated with OpenMM version 7.4 [51] during which the system was simulated in 18 independent replicates, each for 640ns (*i.e.* cumulative time of ~11.5 μs for each FP construct). These runs implemented PME for electrostatic interactions and were performed at 310K temperature under NVT ensemble. In addition, 4fs time-step was used, with hydrogen mass repartitioning and with "friction" parameter set to 1.0/picosecond. Additional parameters for these runs included: "EwaldErrorTolerance" 0.0005, "rigidwater" True, and "ConstraintTolerance" 0.000001. The van der Waals interactions were calculated applying a cutoff distance of 12 Å and switching the potential from 10 Å.

2.2.8. MD SIMULATIONS OF SARS-COV FP INTERACTIONS WITH LIPID MEMBRANES

Interactions of selected two models of the Ca^{2+}-bound wild WT SARS-CoV FP (see Results) with lipid membranes were investigated with atomistic MD simulations. These runs were initiated by placing each of the models in the proximity of a bilayer composed of 3:1:1 POPC/POPG/Cholesterol that had been pre-equilibrated for 25ns as described previously [29].

After the FP-membrane complexes were embedded in a solution box (containing 150 mM Na^+Cl^- salt concentration), each system was equilibrated with NAMD version 2.13 following the same multi-step protocol described above during which the backbone

atoms of the FP as well as the Ca^{2+} ions were first harmonically constrained and subsequently gradually released in four steps. After this phase, the velocities of all atoms of the system were reset, and ensemble MD runs were initiated with OpenMM version 7.4. Each system was simulated in 18 independent replicates, each ran for ~ 1 μs (i.e., cumulative time of ~18 μs for each FP-membrane complex). These runs implemented PME for electrostatic interactions and were performed at 298K temperature under NPT ensemble using semi-isotropic pressure coupling, with 4fs time-steps, using hydrogen mass repartitioning and with "friction" parameter set to 1.0/picosecond. Additional parameters for these runs included: "EwaldErrorTolerance" 0.0005, "rigidwater" True, and "ConstraintTolerance" 0.000001. The van der Waals interactions were calculated applying a cutoff distance of 12 Å and switching the potential from 10 Å.

For all simulations we used the latest CHARMM36 force-field for proteins and lipids [52], as well as the recently revised CHARMM36 force-field for ions which includes non-bonded fix (NBFIX) parameters for Na^+ and Ca^{2+} ions [53].

2.3. RESULTS

2.3.1. GENERATION AND CHARACTERIZATION OF WILDTYPE AND MUTANT SARS-COV SPIKE (S) PROTEINS

Various structural conformations of SARS-coV spike monomer have been solved using Cryo-EM [54]. From these structures, it is apparent that the fusion peptide contains an N-terminal alpha helix, with the hydrophobic LLF residues, and a C-terminal disordered loop known to participate in cysteine-mediated intramolecular disulfide bonding (**Fig 1A**). To identify the SARS-CoV FP's preferred modes of calcium binding, we performed charged-to-alanine substitutions of six highly conserved residues within the

FP sequence (**Fig 1B – C**). We first made single amino acid (aa) substitutions (E801A, D802A, D812A, E821A, D825A, D830A), in the wildtype SARS-CoV FP, which was used as a control. The majority of the negatively charged residues that we mutated are highly conserved across SARS-CoV, MERS-CoV, and SARS-CoV-2 (**Fig 1C**).

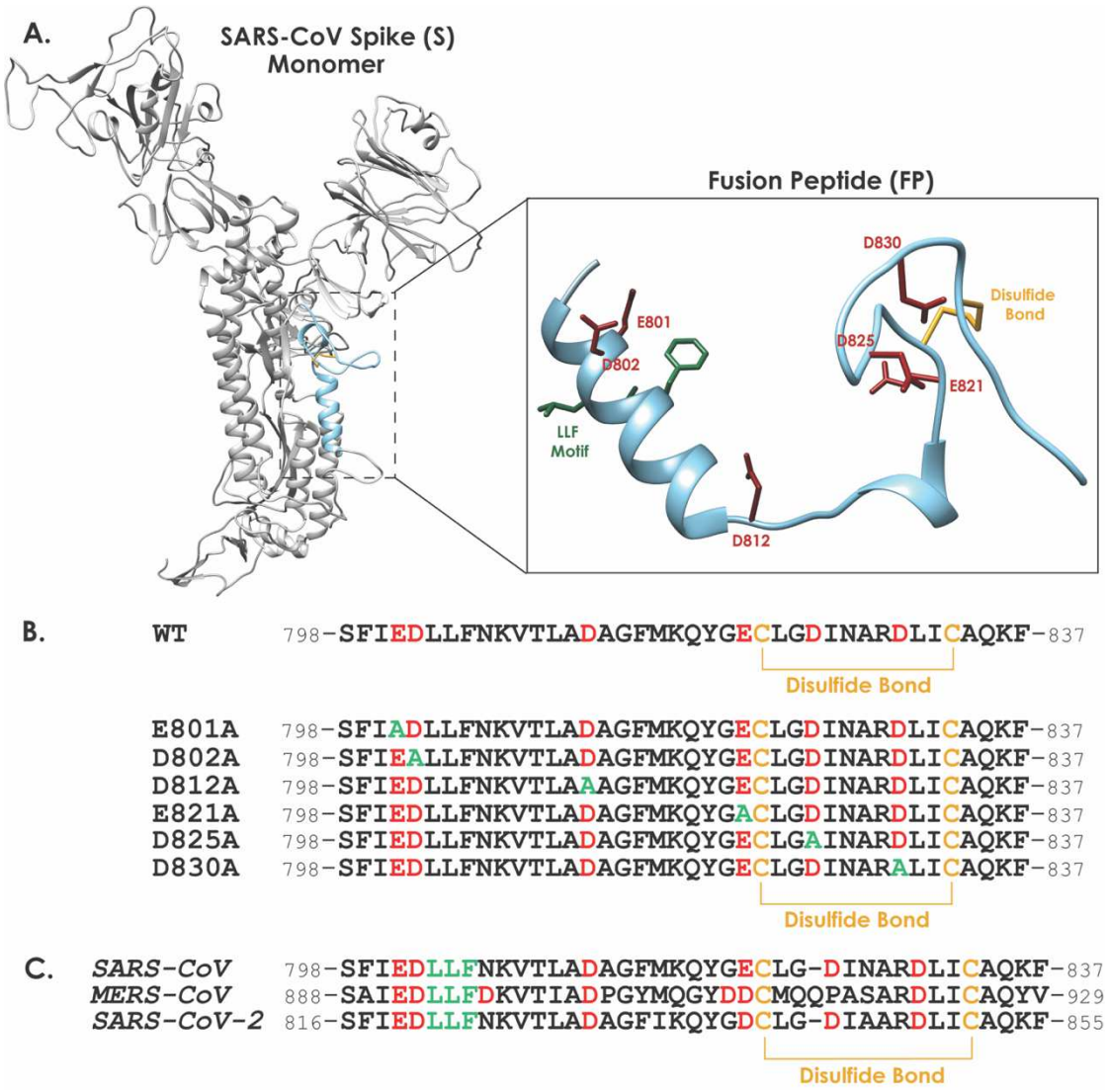

Figure 1. SARS-CoV FP Mutagenesis. (A) SARS-CoV fusion peptide (FP) structure modeled on SARS PDB: 5XLR [54]. Wild type (WT) sequence shows the 40 amino acid sequence (GenBank accession no. AAT74874.1) in the SARS FP. (B) List of single site-directed mutations of charged residues, aspartic acid (D) and glutamic acid (E), with alanine. The charged WT residues and the green

substitution is shown in each position for the single substitution cases. Yellow highlights a critical disulfide bond within the FP that is necessary for its function.

The wildtype and mutant forms of the SARS-CoV were then cloned into the pcDNA expression plasmid in HEK293T cells. Following the confirmation of high transfection efficiency in our cells S protein synthesis, trafficking to the cells' surface, and proteolytic cleavage were all assessed. To assess proteolytic cleavage of the S protein, TPCK-trypsin was added to the cell surface 24 hours after transfection and the S proteins were then isolated by cell-surface biotinylation. Biotinylated proteins were retrieved following cell lysis using streptavidin beads, resolved by gel electrophoresis and immunoblotted using the SARS-CoV S pAb. The resulting immunoblots displayed full length, uncleaved (S_0) and cleaved (S_2) SARS-CoV S protein species migrating at 180 kDa and 80 kDa respectively (**Fig 2A**). SARS-CoV S mutants containing the single mutations D802A, D812A, E821A, D825A, and D830A have comparable steady-state levels of full-length protein in comparison to the wildtype protein, indicating that these mutations in the FP did not impair the synthesis or trafficking of S (**Fig 2A**). Additionally, proteolytic cleavage of the D802A, D812A, E821A, D825A, and D830A mutants occurred following treatment with TPCK-trypsin, indicating that these mutants were able to be primed for downstream fusion events. We observed a high molecular weight species running above the full-length S protein (**Fig 2A, Higher order S**). We have determined that heating samples to 95°C with 5 mM DTT for 10 minutes resolves this higher molecular weight species (**S1 Fig S1**), indicating this species likely results from spike-based protein-protein interactions.

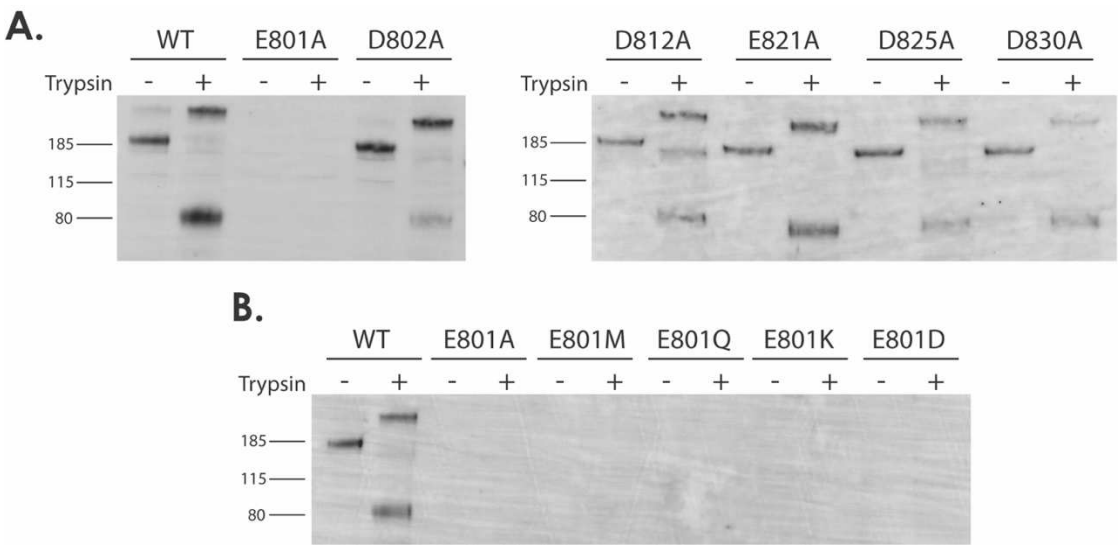

Figure 2. Spike cleavage comparison of SARS-CoV Wild Type (WT) and mutant spike (S). Western blot analysis of SARS S mutant cleavage expression with trypsin (+) and without trypsin (-) treatment. (A) Western blots showing the expression of SARS S mutants. (B) Western blot analysis depicting the expression of SARS E801 S mutants using various amino acid residues. N = 4 (biological replicates).

We were unable to detect steady-state levels of the E801A mutant on the spike immunoblots. To further probe the nature of this residue's importance, E801 was substituted with the larger nonpolar methionine (E801M), polar and uncharged glutamine (E801Q), positively charged lysine (E801K), or negatively charged aspartic acid (E801D). None of these mutations, including the charge mimetic mutant, including the charged mimetic E801D, restored the steady-state levels of the S protein to that of the wildtype protein, indicating the specific requirement of glutamate in this region of the FP (**Fig 2B**).

2.3.2. ANALYSIS OF SARS-COV FP SINGLE POINT MUTATIONS' EFFECT ON S PROTEIN-INDUCED CELL FUSION

We tested the function of the mutant S proteins in a cell-cell fusion assay. To perform this assay, we transiently expressed the WT and mutated S proteins in VeroE6 cells, a

kidney epithelial cell line with high levels of ACE2 expression [24]. 24 hours post-transfection, we induced cell-cell fusion by treating the cells with trypsin to cleave the FP at the S1/S2 site. Syncytium formation (cell-to-cell fusion) was visualized by an immunofluorescence assay (IFA) using fluorescently labeled SARS-CoV S antibody and DAPI stain to identify S-expressing cells that had fused. Syncytia were quantified by counting the number of nuclei per syncytium with the minimum number of 4 nuclei (**Fig 3**). As expected, VeroE6 cells expressing the WT S protein readily formed larger syncytia (**Fig 3A – B**). Conversely, cells expressing the D802A, D812A, E821A, D825A, and D830A mutants all exhibited significantly lower levels of syncytium formation, indicating a defect in cell-cell fusion (**Fig 3A – B**).

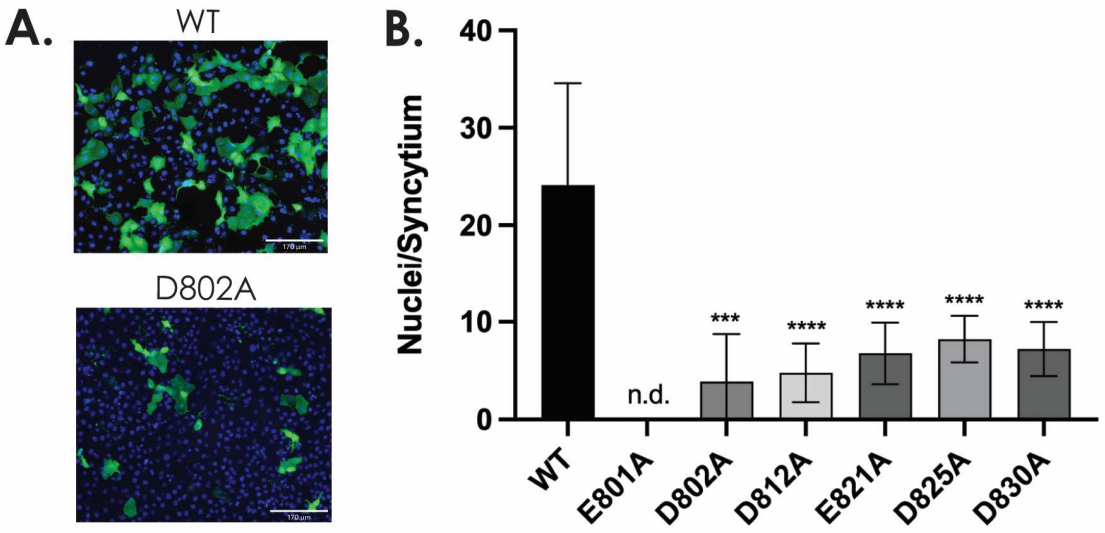

Figure 3. Cell-cell fusion of SARS-CoV WT and mutant S proteins. (A) VeroE6 cells were transfected with the plasmid DNA encoding the respective SARS-CoV S protein variants and grown for 18 h. Vero cells were then treated with TPCK trypsin to cleave SARS-CoV S proteins to induce syncytium formation. Syncytia were visualized using immunofluorescence microscopy by staining the SARS-CoV S protein with an anti-SARS S antibody (*green*) and the nuclei with 4',6'-diamidino-2-phenylindole (DAPI; *blue*). Images were taken at 25X magnification. (B) Quantification of nuclei/syncytia. Nuclei of 9 syncytium from 3 images per sample were counted and averaged. *** denotes significance of $p < 0.001$; **** denotes significance of $p < 0.0001$.

2.3.3. ANALYSIS OF THE SARS-COV FUSION PEPTIDE MUTATIONS EFFECT ON PSEUDOPARTICLE (PP) INFECTION

SARS-CoV is designated a Risk Group 3 Select Agent that requires a specialized biosafety level 3 (BSL-3) setting. Pseudoparticles (PPs) can be used as safe surrogates of live SARS-CoV to enable experimentation in BSL-2 level conditions [45]. To generate replication deficient SARS-CoV pseudoparticles in HEK293T cells, we used a three-plasmid co-transfection system, with plasmids encoding: (1) the full length CoV surface S protein, (2) the murine leukemia virus (MLV) core proteins *gag* and *pol*, or (3) a firefly luciferase reporter gene containing the MLV-MJ RNA packaging signal and flanked by long terminal repeat (LTR) sequences [45]. Upon successful particle entry into host cells, the luciferase reporter RNA transcript is reverse transcribed, integrated into the cell genome and expressed, enabling a measurable readout of pseudoparticle entry. Our previous studies have shown that this approach works well for assessing the infectivity of MERS-CoV S [27] and SARS-CoV S [6, 45] and, more recently, extends to SARS-CoV-2 S [23].

Incorporation of the WT and various mutant S proteins into the SARS-CoV PPs was assessed using immunoblot analysis of collected particles. Pseudoparticles with WT or mutant S proteins (D802A, D812A, E821A, D825A, and D830A) show comparable levels of S protein incorporation (**Fig 4A**). As expected, we did not detect E801A in the SARS-CoV PPs, likely due to its low cellular expression or synthesis.

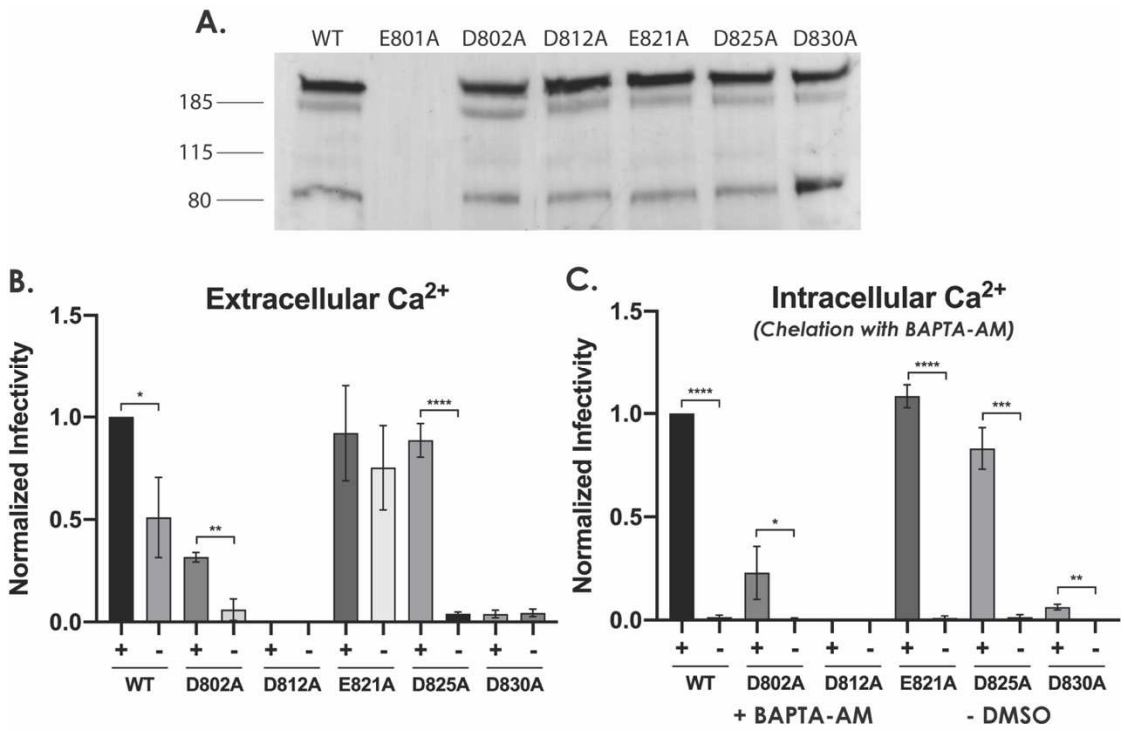

Figure 4. Comparison of SARS-CoV S mutant PP normalized infectivity. (A) Western blot analysis of SARS S mutant PP expression. (B) Infectivity assessment in the presence and absence of extracellular Ca^{2+} under 50 µM EGTA treatment. Notation refers to the net result of the extracellular treatment: (-) refers to the absence of 50 µM EGTA; (+) refers to the presence of 50 µM EGTA. (C) Infectivity assessment in the presence and absence of intracellular Ca^{2+} under 50 µM BAPTA-AM treatment. Notation refers to the net result of the intracellular treatment: (-) refers to the absence of 50 µM BAPTA-AM; (+) refers to the presence of 50 µM BAPTA-AM. The following describes the significance compared to the respective calcium rich conditions (B and C) * denotes significance of $p < 0.05$; ** denotes significance of $p < 0.01$; *** denotes significance of $p < 0.001$; **** denotes significance of $p < 0.0001$.

After confirming the incorporation of the wildtype and mutant spike proteins into the SARS-CoV PPs, we tested their infectivity. As we have demonstrated previously, SARS CoV S WT pseudoparticle infection of Vero6 results in a robust luminescent signal 72 hours post infection, indicating viral entry **(Fig 4B)**. PPs containing the FP E821A and D825A mutations exhibited no significant change in infectivity in comparison to WT particles (**Fig 4B**). In contrast, the D802A, D812A, and D830A

mutant PPs all showed a pronounced decrease in infectivity, with the D812A and D830A mutations causing the greatest reduction in infectivity; D802A and D830A PP infected cells has a 20 – 30-fold reduction in infectivity. These results indicate that mutations in these three highly conserved negatively charged residues in the S protein's FP significantly decrease SARS-CoV PP infectivity under calcium-containing conditions. Importantly, these results indicate that D812 is a key residue in the FP, irrespective of calcium levels, and is required for function of the S protein during viral entry.

We next tested the effect of depleting extracellular calcium on the PPs' ability to infect VeroE6 cells using the chelator, ethylene glycol-bis(ß-aminoethyl ether)-*N,N,N'N'*-tetraacetic acid (EGTA). We have previously studied the effects of calcium on viral infectivity and adopted similar calcium depletion methods to observe an additive effect on PP infectivity in the context of specific FP mutations [6, 27]. Briefly, we treated PPs and VeroE6 cells with 50 μM EGTA prior to infection. Following incubation with the chelating agent, VeroE6 cells were inoculated with WT or mutant S protein containing PPs and incubated for 72 hours. Cells were then lysed and luminescence was quantified as a measure of pseudoparticle infectivity (**Fig 4B**). In support of our previous work [6], depletion of extracellular calcium had a marked effect on WT pseudoparticle infectivity, decreasing it to approximately half that of cells infected with WT PPs in the absence of EGTA (**Fig 4B**). Cells treated with PPs containing either D802A or D825A mutations also exhibited a further drop in infectivity upon the chelation of extracellular Ca^{2+}, with the D825A mutation having the greatest additional reduction in infectivity (**Fig 4B**). The depletion of extracellular calcium had

an additive effect on the decrease in infectivity in the context of specific FP mutations, D802A and D825A. These results suggest that these negatively charged residues in the FP are affected either directly or indirectly by the loss of extracellular calcium, but residual WT PP infectivity from the loss of extracellular calcium may also indicate the intracellular calcium stores were sufficient to mediate viral entry.

We then examined the effect of intracellular calcium depletion on pseudoparticle infectivity by using the cell-permeable calcium chelator 1,2-bis(2-aminophenoxy)ethane- *N,N,N'N'*- tetraacetic acid tetrakis (BAPTA-AM); BAPTA-AM contains four esters groups that allow membrane permeability of BAPTA, the Ca^{2+} chelator, that is activated by intracellular esterases for the capability to chelate only intracellular Ca^{2+} stores [55-57]. This approach was taken to control for the contribution of cell-derived calcium to SARS-CoV entry, as this virus is known to utilize the endosomal pathway in VeroE6 cells [1]. We have previously optimized the concentrations of BAPTA-AM so as not to significantly impact cell viability [6, 27]. VeroE6 cells were treated with 50 μM BAPTA-Am briefly prior to pseudoparticle infection, harvested, and assayed for luminescence as a readout of PP infectivity (**Fig 4C**). Interestingly, depletion of intracellular calcium further reduced the infectivity of WT PPs, compared to the extracellular Caw^{q} chelation (**Fig 4B**). Similar results were observed across all mutants tested: none of the PPs were infectious. In general, this data suggests that depletion of intracellular calcium exerts a more severe effect on SARS-CoV PP infectivity.

From the infectivity data, we deduced that the FP likely uses multiple negatively charged residues to bind to multiple calcium. This is supported by the further decrease

in infectivity of mutant D802A and D825A PPs when extracellular calcium is depleted. Mutating those individual residues do not lead to a complete loss of function since other charged residues in the FP can compensate; however, removal of calcium from the medium mimic s the loss of those additional residues, leading to the inability of the FP to bind to calcium and ultimately a loss in infectivity.

2.3.4. MULTIPLE NEGATIVELY CHARGED RESIDUES MEDIATE SARS-COV FUSION PEPTIDES' CALCIUM BINDING

To test the hypothesis that the FP utilizes redundant charged residues to mediate calcium binding, we created pairwise- and triple-residue substitutions within the S protein's FP. The FP contains two defined regions: the N-terminal region starting just upstream from the S2' cleavage site, termed FP1 (798-819), and the downstream region (820-837) that includes a critical disulfide bond, termed FP2 (**Fig 1**) [42, 58]. Lai *et al.* has reported a stoichiometry of two calcium ions per single SARS-CoV FP [6]. In FP1, the alanine substitutions of residues D802 and D812 rendered their pseudoparticles non-infectious; in FP2, the D830A substitution led to a non-infectious particle. To investigate if individual substitutions of these three residues changed the mode of calcium binding, we created a complete set of their double mutants (E821A/D825A, E821A/D830A, D825A/D830A), and triple mutant (E821A/D825A/D830A) (**Fig 5A**).

We first confirmed the synthesis, trafficking, and cleavability of the mutated S proteins was we have done with the single mutants (**Fig 5B**).–Next, we tested functionality of the S mutants using the previously described cell-cell fusion assay. VeroE6 cells transiently expressing either a double mutant (E821A/D825A,

E821A/D830A, D825A/D830A) or triple mutant (E821A/D825A/D830A) had much smaller syncytia compared to WT expressing cells (**Fig 5C – D**).

We then generated PPs containing the double and triple mutations and assessed the incorporation of the various mutants into the PPs by immunoblotting for the SARS-CoV S protein. The double mutant E821/D830A and D825A/D830A containing PPs incorporated roughly equal amounts of S protein while the triple mutant -containing PP (E821A/D825A/D830A) showed slightly reduced protein levels (**Fig 5C**). The E821A/D825A mutant particle exhibited significantly decreased protein levels indicating that although this mutant was able to be expressed and trafficked to the plasma membrane, incorporation into the PPs was somehow defective. We acknowledge the general low protein levels of the double and triple S mutants in our PPs as being a potential confounding variable.

We then infected VeroE6 cells with the WT and mutant S protein PPs to investigate if multiple mutations in negatively charged residues of the FP caused a more pronounced decrease in infectivity. As was previously demonstrated, WT S PPs are able to infect VeroE6 cells, with subsequent depletion of extra- or intra-cellular calcium causing a partial or complete loss of infectivity, respectively (**Fig 5F – G**).

Infectivity was dramatically reduced for all mutants in comparison to WT S PPs, irrespective of extra- and intracellular calcium levels (**Fig 5F – G**). This data supports the hypothesis that the SARS-CoV FP contains multiple sites of calcium interaction, which when mutated, results in a nonfunctional S protein. More specificially, our results here reinforce the conclusion that the two calcium sites in the FP are necessary for

SARS-CoV PPs entry; E801, D802, and D812 residues in the FP1 domain are essential, while calcium interaction in FP2 appears to be flexible between E821, D825, and D830.

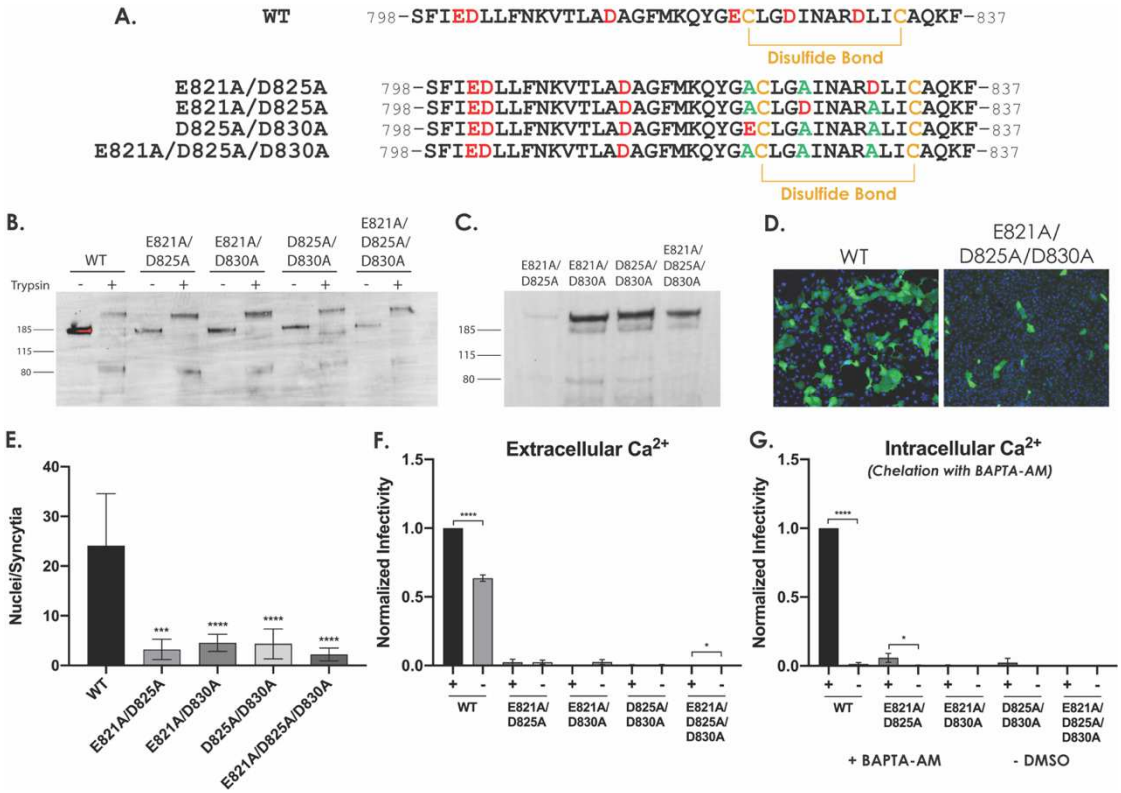

Figure 5. Assessing the calcium coordination between E821, D825, and D830. *A*. Double and triple mutations performed on the FP2 domain to further study the hypothesized alternating coordination with D830. *B*. Western blot of the mutant S protein to show successful induction of the mutants in S protein synthesis in HEK293T cells. *C*. Western blot of the SARS S mutant PP to show expression of mutant S into PPs. *D*. Cell-cell fusion assay of mutant S proteins. *E*. Quantification of nuclei per syncytia. *F*. Assessing PP infectivity when extracellular calcium is depleted. Notation refers to the net result of the extracellular treatment: (+) refers to the presence of extracellular Ca2+; (-) refers to the absence of Ca^{2+} due to the presence of 50 µM EGTA. *G*. Assessing PP infectivity when intracellular calcium is depleted with 50 µM BAPTA-AM. Notation refers to the net result of the intracellular treatment: (+) refers to the presence of intracellular Ca^{2+} with no BAPTA-AM; (-) refers to the depletion of Ca^{2+} due to the presence of 50 µM BAPTA=AM. The following describes significance to the WT (*E*.) or respective calcium rich conditions (*F*. & *G*.) based on the following: * denotes significance of $p < 0.05$; *** denotes significance of $p < 0.001$; **** denotes significance of $p < 0.0001$.

2.3.5. MOLECULAR DYNAMICS (MD) SIMULATIONS IDENTIFY MODES OF CA^{2+} BINDING TO SARS-COV FP

The effects that the various S mutants have on SARS CoV pseudoparticle infectivity suggests that the FP contains multiple sites of Ca^{2+} binding that are required for viral entry. This confirmed requirement of $Ca^{2+}$for FP function prompted an analysis of the predicted modes of Ca^{2+} binding in the wildtype and mutant SARS-CoV FPs. To this end, we carried out extensive atomistic molecular dynamics (MD) simulations of all the SARS-CoV FP constructs studied here (see **Methods**). To monitor the spontaneous binding of Ca^{2+} to the FP, we collected 18 independent MD trajectories of 640ns in length for each construct. Following the analysis protocols described recently for SARS-CoV-2 FP simulations [29], the various modes of interactions between the SARS-CoV FP and Ca^{2+} ions were assessed in the trajectories by monitoring: i) the distances between the Ca^{2+} ions in solution and the side chains of all acidic residues in the peptide; and ii) the pairwise distances between the side chains of all acidic residues. Summarized in **Fig S3** are the observed events of simultaneous association of two Ca^{2+} ions with various pairs of FP residues in the individual trajectories of the WT and the mutant systems (see *red* and *blue* rectangles). The combined statistics for each construct (i.e., the total number of binding events for different pairs of residues) are summarized in **Fig 6**.

Results in **Fig 6** show the modes of Ca^{2+} coordination in the WT protein, identifying the most frequent modes involving residue pairs E821/D825 (5 out of 18); E801/D802 and E801/D830 (4/18 each); and D812/E821 (2/18). Notably, a similar pattern of coordination preference was observed in our recent computational studies of Ca^{2+}

association with SARS-CoV-2 FP [29]. Moreover, simultaneous binding of Ca^{2+} ions to the SARS-CoV-2 FP residue pairs equivalent to E801/D802 and D812/E821, produced the peptide conformations prone to membrane penetration. In contrast, conformations that stabilized Ca^{2+} binding to residues equivalent to the E821/D825 pair did not enable sustained bilayer insertion.

MD simulations of the SARS-CoV FP constructs with single mutations with decreased cell fusion activity (i.e., E801A, D802A, D812A, and D830A in **Fig 6**) showed that only the Ca^{2+}-coordination mode involving the E821/D825 pair persists, but not the one involving the D812/E821 pair. Conversely, in the SARS-CoV FP single mutants found to maintain WT-like fusion activity (i.e., E821A and D825A in **Fig 6**) we did not observe the E821/D825 binding mode. In these function-preserving mutants we identified other modes of Ca^{2+} binding that are enhanced compared to the WT system: E801/D802 (for E821A) or E801/D830 (for D825A).

For the SARS-CoV FP constructs with multiple mutations our MD trajectories revealed an overall reduced Ca^{2+} binding ability (**Fig 6** and **Fig S4**), consistent with our experimental findings that (i) these constructs are severely defective in the cell-cell fusion and infectivity assays (**Fig 5D – E**), and (ii) their function does not depend on the levels of either extracellular or intracellular Ca^{2+} (**Fig 5F – G**).

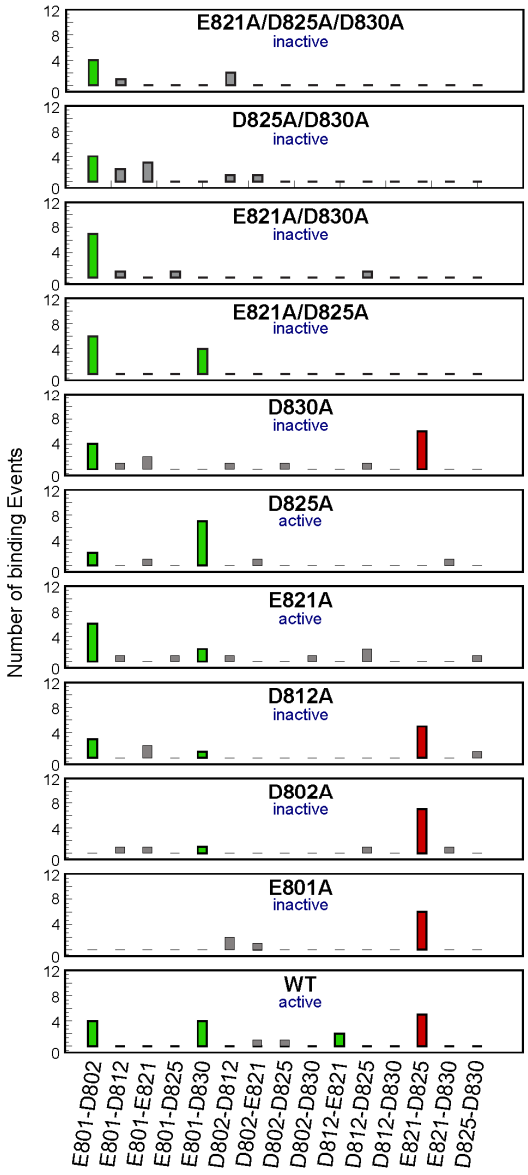

Figure 6. Modes of Ca^{2+} binding to SARS-CoV FP. Number of Ca^{2+} binding events to different pairs of anionic residues in SARS-CoV FP in the simulations of the WT and the mutant constructs (labeled in each panel). The experimentally measured phenotypes for each construct are shown (active or inactive). The mode of Ca^{2+} ion association predicted to be inhibitory for membrane insertion (E821-D825) is shown in *red*, and the modes of Ca^{2+} association predicted to facilitate membrane insertion are depicted in *green* boxes.

2.3.6. SARS-COV FP PROPENSITY FOR MEMBRANE INSERTION IS REGULATED BY MODES OF CA^{2+} BINDING

Overall, the above computational results reveal that the Ca^{2+} binding patterns of SARS-CoV FP are very similar to those of SARS-CoV-2 FP. On this basis, membrane insertion of the SARS-CoV FP could be expected to be enhanced by the modes of Ca^{2+} binding involving the E801/D802 and D812/E821 pairs of residues, and to be reduced by the ones involving the E821/D825 pair.

To test this premise, we carried out MD simulations of two models of the WT SARS-CoV FP spontaneously associating with the lipid membrane (see **Methods**). In one, the peptide was interacting with 2 Ca^{2+} ions at the E801/D802 and D812/E821 sites (Model 1), and in the second, 2 Ca^{2+} ions were bound to the E801/D802 and E821/D825 pairs (Model 2). Each structure was simulated in 36 independent replicates, each run for ~0.9-1.0μs (see **Methods**).

Analysis of these trajectories revealed that, indeed, Model 1 extensively penetrated the membrane, while the membrane insertion of the Model 2 was negligible. This can be seen from the plots presented in **Fig 7** comparing frequencies of membrane insertion for each SARS-CoV FP residue in the simulations of Model 1 and Model 2 structures. The membrane insertion was quantified by monitoring the z-coordinate of the C_α atom of each residue in the peptide. A residue was inserted into the membrane if the z-distance between its C_α atom and the second carbon atom in the tail of a POPC lipid (atom C22 in CHARMM36 notation) was <5Å. As shown in **Fig 7A**, in Model 1, the N-terminal FP1 segment of the fusion peptide shows strong propensity for bilayer insertion, while in Model 2 the insertion is minimal (**Fig 7B**).

The detailed analysis of the individual trajectories in the Model 1 set revealed two distinct modes of bilayer penetration for SARS-CoV FP, similar to our findings for the SARS-CoV-2 FP. Thus, the Model 1 construct penetrates the bilayer either with its N-terminal LLF motif (**Fig 7C**) or with the more centrally located hydrophobic F815-M816 segment (**Fig 7D**). Interestingly, the two insertion modes appear to alternate which Ca^{2+} ion is neighboring the inserted portion. Thus, when the LLF is inserted, the Ca^{2+} ion associated with the neighboring E801/D802 residues is bound to the membrane while the other Ca^{2+} binding site (D812/E821) is situated away from the membrane surface (see snapshot in **Fig 7C**). In case of the F815-M816 insertion, the position of the Ca^{2+} binding loci with respect to the membrane is reversed – the one associated with the D812/E821 pair is membrane-bound, while the E801/D802 pair is located farther from the bilayer (snapshot in **Fig 7D**). We also note that in both cases, the remaining anionic residues in the peptide (*i.e.* the ones not engaged with the Ca^{2+} ions) are either solvent exposed (D830) or engaged with electro-neutralizing interactions with neighboring basic residues (D825/R829, **Fig 7C – D**). These results support a mechanistic model in which membrane penetration of the SARS-CoV FP is significant only for specific modes of Ca^{2+} binding to the peptide, i.e., to the E801/D802 and D812/E821 pairs of conserved acidic residues. Moreover, Ca^{2+} binding at the E821/D825 pair is predicted to inhibit membrane insertion.

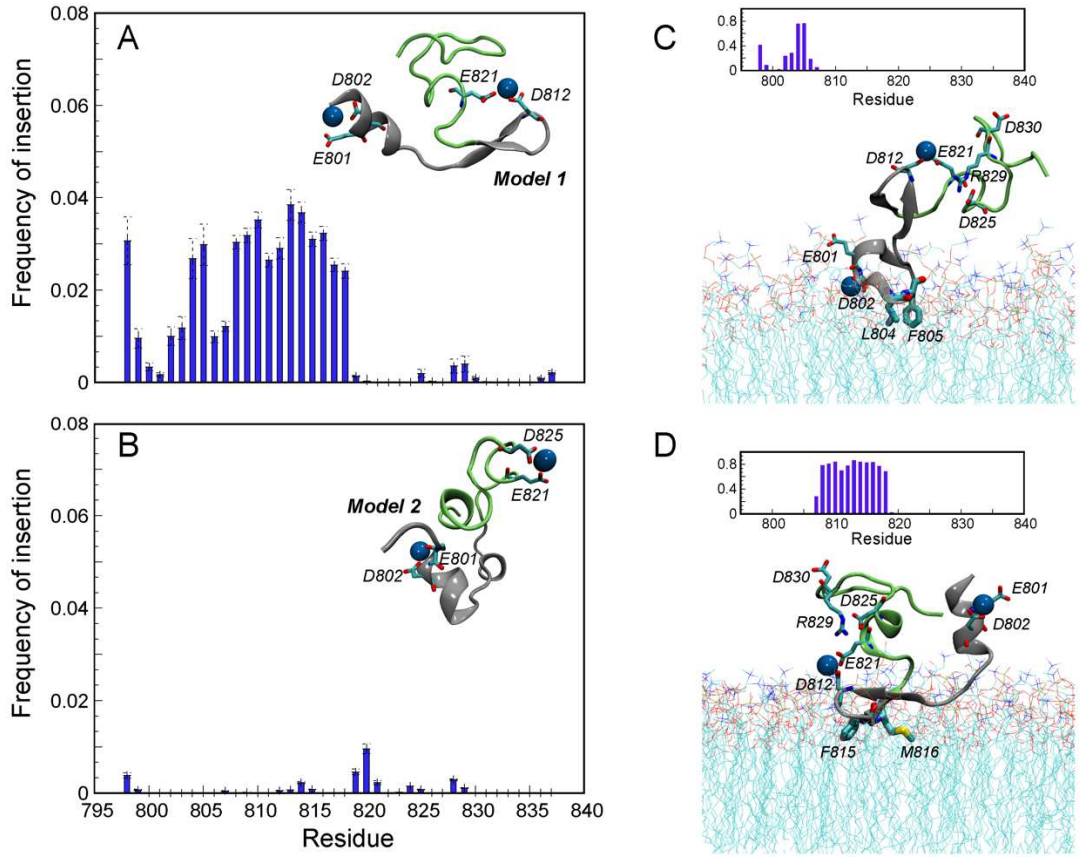

Figure 7. Membrane insertion for FP1 and FP2 domains of SARS-CoV FP. *A-B*. Frequency of membrane insertion for each residue of SARS-CoV1 FP in the MD simulations of Model 1 (*A*) and Model 2 (*B*) constructs (differing in the mode of Ca^{2+} coordination, see text). The snapshot insertions in the panels show the corresponding structures. Ca^{2+} coordinating anionic residues are highlighted by licorice rendering; Ca^{2+} ions are shown as blue spheres. The FP1 and FP2 parts of the fusion peptide are colored in silver and lime, respectively. *C-D*. The same frequency calculations but done separately for two representative trajectories in Model 1 set in which the observed membrane insertions involved the N-terminal LLF motif (*C*) and the more centrally located (F815-M816) hydrophobic segment (*D*). The corresponding snapshots illustrate structural features of these two distinct insertion modes highlighting (in licorice) positions of the anionic residues, the hydrophobic residues penetrating the membrane, and R829 residue interacting with D825. Same color code as in panels *A-B*.

2.4. DISCUSSION

The resurgence of pathogenic human coronaviruses brings about an immediate need for improving countermeasures to combat these global health threats. Increasing our

knowledge of the mechanisms of viral entry is essential to develop broad-spectrum vaccines and antivirals. Viral entry is a critical step in the viral life cycle that is mediated by the S viral protein [36, 59, 60]. The S protein's FP is responsible for mediating viral and host cell membrane fusion. This region is highly conserved across the *Coronaviridae* viral family and understanding it how it functions may lead to the development of more broadly acting therapeutics. Previous work has highlighted the role that cations play in viral fusion, specifically Ca^{2+}, as their electrostatic interactions with negatively charged residues in the fusion peptide promote membrane fusion, leading to higher infectivity [2, 3, 6, 27, 28]. Lai *et al* has proposed that two Ca^{2+} ions were needed to interact with SARS-CoV FP; in each of the subdomains (FP1 and FP2), one Ca^{2+} coordinates two negatively charged residues to allow the FP to adopt a conformation that promotes membrane insertion [6]. In our work, we identify the residues in the SARS-CoV FP responsible for interacting with calcium in configurations that correspond to the measured activities. The infectivity studies and MD simulations revealed the modes of interaction of the E801, D812, and D830 residues with Ca^{2+} interaction and the manner in which their mutations to alanine in various combinations can result in the measured decreases in viral infectivity, and further sensitization of the FP upon calcium depletion, indicating the importance of Ca^{2+} mediated interactions with multiple negatively charged residues present to FP function (**Fig 6**).

To interrogate the requirement of the negatively charged residues in the SARS CoV fusion peptide for its function, we first made single charge-to alanine substitutions in those residues (**Fig 1**). Following transient expression of these mutants in VeroE6 cells, we confirmed that mutants D802A, D812A, E821A, D825A, and D830A were

synthesized, accumulated to levels comparable to the WT protein, and were trafficked to the plasma membrane using a cell surface biotinylation assay (**Fig 2**). The majority of the FP mutants assayed exhibited cleavage following treatment with trypsin, indicating the accessibility of the S1/S2 cleavage site. The E801A mutant was not detected on our immunoblots and further attempts to understand this occurrence through additional substitutions with charge mimetics did not result in the detection of this mutant. We hypothesize that the absence of glutamate at position 801 in the fusion peptide causes a loss in protein stability and further work is needed to determine the significance of this residue in the fusion peptide.

We next tested the fusion competency of the single FP mutants we had created using a syncytia assay, which utilizes fusion events in cells transiently expressing the FP as a surrogate readout of FP activity. Most of the single FP charged-to-alanine mutants the were detected on the spike immunoblot (D802A, D812A, E821A, D825A, and D830A) exhibited a pronounced fusion defect, as evidenced by the low number of fused VeroE6 cells, or syncytia, that were observed (**Fig 3**). Taken together, this data suggest that the highly conserved, negatively-charged residues within the FP individually contribute in a non-redundant manner to the function of the fusion peptide. However, due to the limitations and variability of the syncytia assay, we chose to use SARS-CoV PPs to mimic a more in vivo-like system to examine the functionality of the various FP mutants. We confirmed the incorporation of the WT and single-charged-to-alanine mutant FPs into the pseudoparticles (**Fig 4A**). Nearly all FP mutants generated (E801A, D802A, D812A, E821A, D825A, and D830A) were present in the SARS-CoV PPs; the E801A mutant was not detected.

We then proceeded to test the requirement of extracellular calcium on the infectivity of our FP-containing PPs by treating the cells with EGTA, a calcium-preferring chelator, prior to infection. Removal of extracellular calcium still rendered the WT S particles, indicating that intracellular calcium stores may still be sufficient for SARS-CoV PP viral entry (**Fig 4b**). Interestingly, PPs containing either the D802A or D825A mutant showed a further reduction in infectivity when the extracellular calcium was depleted. This suggests that multiple negatively charged residues in the FP are involved in calcium binding. While the loss of a single negative charge may not be sufficient to completely disrupt infectivity, removal of extracellular calcium mimics the loss of additional electrostatic interactions needed for FP function, resulting in a further decrease in infectivity. Pseudoparticles containing either the D812A or D830A FP mutant were essentially non-infectious in the presence or absence of extracellular calcium. These results implicate residues D812A and D830A in FP function; however, their specific roles as they relate to calcium cannot be teased apart in this system.

We also depleted intracellular calcium levels using the cell permeable calcium chelator BAPTA-AM, to control for the cellular contribution of calcium during pseudoparticle fusion and viral entry. BAPTA-AM is a cell-permeant calcium chelator that specifically depletes intracellular calcium levels. Following treatment with BAPTA-AM, WT and mutant PPs are no longer infectious (**Fig 4B – C**), indicating that intracellular calcium may contribute to viral entry processes. We propose that chelation with EGTA likely removed the majority of extracellular calcium causing a 50% reduction in infectivity of WT FP-containing pseudoparticles; however, upon viral and host cell membrane fusion, intracellular calcium may supply this cation to the FP at this

critical interface. Hence, the partial reduction in viral infectivity in the presence of EGTA and then the complete loss of infectivity in the presence of BAPTA-AM. By chelating intracellular stores, this further confirmed the necessity of intracellular calcium for successful SARS-CoV PP viral entry in VeroE6 cells. It should be noted in the VeroE6 cells, SARS-CoV predominantly enters via the endosomal pathway due to the absence of TTSPs. It is important for us to acknowledge that we cannot rule out the potential impact depletion of intracellular calcium may have on the integration, expression, or synthesis of our reporter transgene. Cell viability assays were performed to optimize the concentrations of both chelators that we used in this study [6]; however, we must exercise caution when interpreting these results and acknowledge this caveat. Additionally, future studies will need to be performed to assess the specific effect of depleting intracellular calcium as it relates to the endosomal pathway of SARS-CoV entry.

Given that the results from our infectivity assay suggested the involvement of multiple calcium-binding residues in the fusion peptide, we then generated double mutants (E821A/D825A, E821A/D830A, D825A/D830A) and a triple mutant (E821A/D825A/D830A) of the FP (**Fig 6A**). We validated the expression, synthesis, and cell surface localization of these mutants, as well as their ability to be cleaved by trypsin (**Fig 6B**). As with the single mutants, we observed a fusion defect in VeroE6 cells transiently expressing all these mutant constructs, evidenced by the limited syncytia formation in comparison to cells expressing the WT FP (**Fig 6C – D**). When then assayed the infectivity of these mutants using the previously described

pseudoparticle infectivity assay. The double mutants E821A/D830A and E825A/D830A and a triple mutant E821A/D825A/D830A were all incorporated into the pseudoparticles; the E821A/D825A was not fully incorporated (**Fig 6E**). If the FP binds calcium using more than one negatively charged residue, then pseudoparticles containing the double or triple charge-to alanine mutants should exhibit a further decrease in infectivity. In comparison to WT FP-containing pseudoparticles, the FP double mutants E821A/D830A and D825A/D830A and a triple mutant E821A/D825A/D830A we assayed showed a complete loss in infectivity. Because the FP double mutant E821A/D825A was not fully incorporated into the pseudoparticles, we could not fully assess the impact of these mutations on FP function; however, the low number of syncytia observed in cells expressing this mutant suggests these residues are important for FP function. In summary, these results support the hypothesis that the SARS-CoV fusion peptide requires multiple negatively charged residues to bind to calcium during viral entry. Specifically, these data implicate residues as being critical to FP function through calcium-mediated interactions.

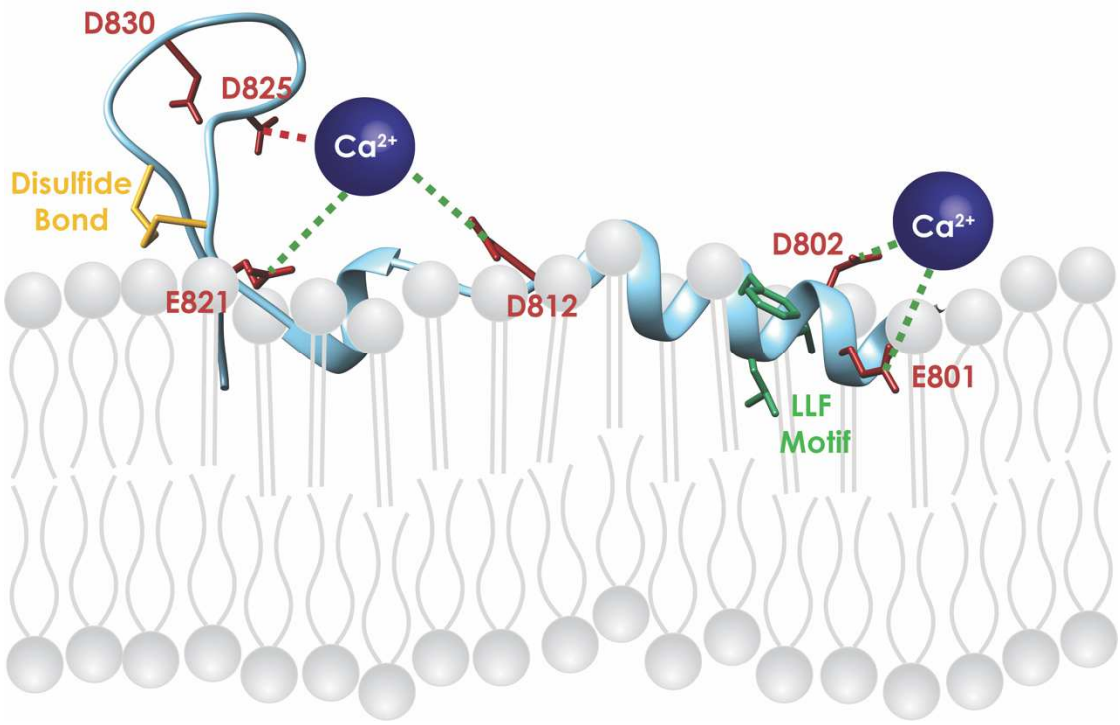

Figure 8. Revised model of CoV FP interaction with a lipid bilayer. This model summarizes the data obtained from the work and highlights the role of Ca2+ with the key charged residues in the pre-fusion form of the fusion peptide (PDB: 5XLR), depicting the insertion of the FP1 domain with E801/D802 binding and neutralization of D812 by alternating binding between E821 and D825.

The MD simulations of the Ca^{2+}-loaded peptide with the membrane illuminated the way Ca^{2+} -FP binding may affect FP function. Exploring the probability of each FP residue interacting with the membrane in the identified Ca^{2+}-binding modes (**Fig 7**) reveals the preferred mode of peptide insertion to be with the N-terminal end interacting with a calcium ion coordinated by residues E801 and D802. The depth of insertion and the determinant role of the Ca^{2+} ion in facilitating membrane insertion are identical to the findings for the SARS-CoV-2 peptide, and in agreement with the experimental measurements of SARS-CoV FP membrane insertion by Lai *et al* [6, 27, 28]. That Ca^{2+}

interacts with the same highly conserved, charged residues in the FPs of SARS-CoV and SARS-CoV-2 is not surprising.

Results from our computational modeling of SARS-CoV FP-membrane interactions in the presence of Ca^{2+} show that the propensity of the SARS-CoV FP for membrane insertion is dictated by specific modes of Ca^{2+} binding. The Ca^{2+} binding mode that enables the most sustained membrane penetration involves the initial association of the peptide with the bilayer through a Ca^{2+} binding site located near the N-terminus of the peptide. This site (E801/D802) is made accessible following enzymatic cleavage and is inserted into the membrane via the insertion of the juxtaposed hydrophobic segment (the LLF motif). In this process, all anionic residues of the peptide are either engaged with Ca^{2+} ions, with neighboring basic residues, or remain solvent exposed away from the membrane. Based on the preferred modes of Ca^{2+}-loaded FP interaction with the membrane, we propose that the binding of Ca^{2+} following S protein cleavage at the S2' site creates an energetically feasible membrane insertion process (**Fig 7A**) composed of the following steps: (1) steering of the peptide towards the bilayer surface; (2) exposure of the hydrophobic layer of the membrane of the conserved N-terminal LLF motif of the FP anchored by the Ca^{2+} interactions with the phospholipid headgroups; and (3) shielding of the anionic residues of the peptide by the preferred inserting conformation of the FP to prevent their negative charge from interfering with membrane insertion. These three components became evident from the analysis of the MD simulation trajectories presented here for the SARS-CoV FP and bear a very high similarity to results from computational studies of the SARS-CoV-2 FP (PMID: 33631204).

Remarkably, in both the SARS-CoV-2 FP simulations [29] and here, we observed a Ca^{2+} binding mode that inhibits long-lasting membrane insertion. In this mode Ca^{2+} association with the E821/D825 pair (corresponding to the D839/D843 in SARS-CoV-2 FP) positions the LLF motif near the negatively charged D812 residue at the membrane surface (**Fig 7B**). This eliminates the favorable effect of the negative charge screening by the Ca^{2+}, so that the peptide bilayer encounters are transient and do not lead to penetration by the LLF motif. This mechanistic model, which highlights the role of the positioning of D812 residue in specific Ca^{2+} binding modes, is supported by our findings for the SARS-CoV S mutants, as it was previously found to be an impactful mutation in the SARS-CoV FP [42]. A recent study from Koppisetti *et al* asserts that a Ca^{2+} may be binding to D843/D849 in SARS-CoV-2 FP (corresponding to D825/D830 in SARS-CoV FP), however, as shown from the simulations in this study and Khelashvili *et al*, there is a high likelihood that second Ca^{2+} ion will bind to D812/D821 (corresponding to the D830/D839 in SARS-CoV-2 FP) for the maximal membrane penetration [29, 44]. Recent NMR studies regarding the membrane interaction with the fusion peptide still has yet to be fully resolved as current models use bicelles [44] and micelles [61], which do not completely capture the composition of the bilayer as was done for the computational modeling shown here; though the model of membrane insertion proposed by Koppisetti *et al* [44] most aligns with our proposed CoV FP interaction with bilayer (**Fig 8**). Thus, as shown in **Figs 6 and 7**, mutations that creates a high propensity for the Ca^{2+} binding mode involving the E821/D825 pair, stabilize peptide conformations that are non-productive for membrane penetration and are found here to inactivate the FP (**Fig 6**).

Interestingly, though our computational studies did not confirm the role of D830 with Ca^{2+}, our biological studies still reaffirmed its importance in the FP. Current studies on SARS-CoV-2 S protein classified the disordered portion of the FP in the FP2 domain as the FPPR (fusion peptide proximal region), which includes the charged residues D839/D843/D848 or E821/D825/D830 equivalent in SARS-CoV FP [29, 62]. This FPPR region was determined to be important, as it binds to the RBD through the CTD1, and maintains the closed pre-fusion S trimer [62]. This is due to the tight packing around the disulfide bond reinforced by a bond between K835 and D848 (K817 and D830 in SARS-CoV FP). The equivalent residue in SARS-CoV FP, based on biological studies, is a critical residue [62]. Mutating D830 removes the binding partner of K817, thereby loosening the 'knot' of the structured FPPR in maintaining the closed form of the trimeric S protein [62]. Without the reinforcements, we may lose the optimal structural conformation of the S protein upon receptor binding to expose the S2' cleavage site to promote successful proteolytic cleavage [30].

More broadly, the E801 and D830 residues are conserved within the CoV family and the D812 residue is conserved within betacoronaviruses [6, 42]. The implication is that calcium interactions are a conserved mechanism that serves to better position the FP for membrane insertion. Different coronaviruses exhibit different requirements for calcium; MERS-CoV binds to one Ca^{2+} ion in its FP1 domain [27], thus, it is important to investigate the role of Ca^{2+} and FP interactions across the CoV family. The conservation of calcium-binding residues in the FP of many coronaviruses suggests that the CoV fusion mechanisms can be potential targets for broad-spectrum antiviral drugs [4, 63, 64]. Repurposing FDA-approved calcium channel blocking (CCB) drugs to

inhibit CoV entry, particularly for SARS-CoV-2, is one option worth exploring. Recent studies have shown that the CCB felodipine is a potential candidate to inhibit SARS-CoV-2 entry [63]. CCBs can target conserved viral functions, providing a rapid solution to address new and future SARS-CoV-2 variants. It will be important to identify the mechanisms of CCBs CoV inhibition, as they may directly inhibit a viral target or indirectly inhibit viral entry by affecting host cell processes

In this study, we elucidate the relationship between highly conserved residues in the SARS CoV FP and the critical role they have in coordinating calcium binding to facilitate viral entry. Interestingly enough, recent SARS-CoV-2 variants have arisen as part of Clade 20A that contain a D839G or D839Y mutation (E821 equivalent in SARS-CoV), with this mutation predicted to affect FP-Ca^{2+} interactions [65-67]. To date, it is not known if there is any selective advantage to the virus conferred by this mutation or whether the emergence of these variants simply represents a founder effect. Overall, more details to be investigated to fully understand the role calcium plays in the CoV FP function and its effects on viral pathogenesis.

Regarding the overall role calcium plays during SARS-CoV entry, our data points to the necessity of intracellular, as well as extracellular, calcium for viral entry. Loss of extracellular results in a 50% reduction in PP infectivity, while the loss of intracellular calcium rendered noninfectious PPs. Together with the MD simulations, we propose a model of SARS-CoV viral entry mediated in part by calcium. In this model, the spike protein upon S2' cleavage, the FP is exposed and is stabilized by binding to calcium. We believe that the residues that likely mediate these essential interactions with calcium are E801/D802 and D812/E821. Stabilization of the FP is likely critical for host

membrane insertion, given the unstructured and flexible FP2 loop in this peptide. We hypothesize that calcium interaction helps stabilize the FP structure prior to membrane insertion; in the absence of a single residue, the FP may have functional redundancy in that is can use other negatively charged residues in close proximity. Future studies should focus on the interplay calcium has during the viral entry process in the context of the endosomal pathway to isolate the instance when calcium interaction takes occurs and how depletion of intracellular calcium arrests the viral entry pathway.

2.5. ACKNOWLEDGEMENTS

This work was supported by National Institute of Health research grant R01AI35270, National Science Foundation RAPID grant 2027070 and Fast Grant from the Mercatus Center at George Mason University. TT is supported by the National Science Foundation Graduate Research Fellowship Program under Grant No. DGE-1650441 and the Samuel C. Fleming Family Graduate Fellowship. We would like to thank members of the Daniel, Whittaker, and Abbott groups as well as the Weinstein group at Weill Cornell for helpful discussions.

CHAPTER 3
FUTURE DIRECTIONS

3.1. CALCIUM CHANNEL BLOCKERS: A POSSIBLE VENUE OF COVID-19 TREATMENTS

3.1.1. MOTIVATION & RATIONALE

Though there has been significant success in vaccine development to fight against the ongoing COVID-19 pandemic, there is a pressing need to continue to search for alternative therapeutic treatments to mitigate against the rise of SARS-CoV-2 variants. Previously studies highlighted the importance of calcium during membrane fusion with the coronavirus spike (S) protein, specifically the fusion peptide of SARS-CoV [6], MERS-CoV [27], and SARS-CoV-2 [28, 29]. For all cases, depletion of either intracellular or extracellular Ca^{2+} with chelating agents, BAPTA-AM or EGTA, resulted in partial or full inhibition of viral entry and fusion. Most recent computational simulations suggest that presence of two calcium ions, in the case of SARS-CoV and SARS-CoV-2, are necessary to bind to the fusion peptide (FP) to promote its most energetically favorable conformation for the maximal penetration into the host cell membrane. The significant role of Ca^{2+} during CoV viral entry opens the possibility of utilizing FDA-approved $_{L}$-type calcium channel blockers (CCBs) as potential therapeutics for COVID-19 treatment [27, 68]. This study, led by our team, found amlodipine, felodipine, and nifedipine the most effective to inhibit SARS-CoV-2 growth, namely felodipine and nifedipine being the most promising *in vivo* therapeutic candidates. There is evidence of CCBs blocking other viral infections during viral entry, such as influenza A, Ebola virus [69], Hepatitis C, Dengue virus, and West Nile virus

[26, 70]. The exact mechanism of inhibition yet remains to be determined, whether during viral fusion or assembly within the virus or cellular regulatory mechanism.

The interconnected relationship between Ca^{2+} and viruses is well-studied, however, limited regarding CoV. To gain a holistic understanding of the role of Ca^{2+} throughout the CoV viral cycle, we must study viroporins and endo-lysosomal Ca^{2+} ion channels.

In many cases, viroporins act as regulatory switches to preserve inactive virions during viral assembly and trigger to induce membrane fusion during viral infection. The influenza M2 protein, for instance, protects the acid-sensitive HA protein from prematurely activating during viral assembly and upon viral entry, initiates an influx of H^+ inside the viral particle to trigger membrane fusion [71, 72]. In a similar fashion, the manipulation of Ca^{2+} homeostasis may also be regulated by SARS-CoV(-2) E and 3a. Recent studies imply SARS-CoV-2 E protein may play a role during viral replication as its presence bends the surrounding membrane to promote viral budding, in addition to a reduction of intracellular Ca^{2+} expression of SARS-CoV-2 E protein in cells which may aid the viral escape from the host cell [71-74]. Though there is limited understanding on ORF3a, the calcium permeable nature of both E and 3a heavily suggests the "switch" mechanism of these viroporins: (1) influx of Ca^{2+} ions during viral assembly lowers cytosolic Ca^{2+}, hampering innate immune responses of protein trafficking pathways to escape the host cell, and (2) efflux of Ca^{2+} during membrane fusion elevates cytosolic Ca^{2+}, ultimately triggering the cellular apoptotic pathway.

As previous studies have demonstrated the direct role Ca^{2+} has on CoV membrane fusion, it is important to investigate endolysosomal Ca^{2+} ion channels to understand their contribution to the viral fusion pathway for a holistic mechanistic understanding

on the impact CCBs has on CoV entry. The endocytic pathway is influenced by many ion gradients, particularly Ca^{2+}. The increased levels of Ca^{2+} in the endosome signifies the maturation into a lysosome as its acidic pH is necessary to maintain high [Ca^{2+}] [26]. Following which, the activation of Ca^{2+} permeable ion channels, TPC1 and TPC2, in endo-lysosomes induces the efflux of Ca^{2+}, triggering membrane fusion and release of viral contents into the cytosol [75]. Previous studies on other viruses (i.e. Ebolavirus), however, show promise in the re-purposing of FDA-approved L-type calcium channel blockers (CCB) on inhibiting TPCs activity to prevent viral membrane fusion, shedding light the CCB mechanism of action during viral entry [69].

Ca^{2+} ions are essential signaling molecules for not only the host cell machinery, but also the viral life cycle. Studies have shown the essential role of Ca^{2+} on CoV membrane fusion, which opens up the potential of utilizing CCBs as possible COVID-19 treatments. There is limited knowledge on the mechanistic inhibitory effects of CCBs on CoV entry. By studying Ca^{2+} permeable viroporins and endolysosomal ion channels, we gain more insight on how Ca^{2+} influences the CoV life cycle.

3.1.2. RELEVANT BACKGROUND

3.1.2.1. VIROPORINS AS ION CHANNELS

Viroporins are small hydrophobic viral proteins with ion channeling activity that play a role in many viral processes, such as modifying host membrane permeability for increased viral assembly and release. Compared to many CoVs, the SARS-CoV and SARS-CoV 2 genomes encode for 3 putative viroporins: proteins 3a, E, and 8a; two of which, 3a and E, are highly conserved and required for maximal SARS-CoV replication and virulence [73, 76]. Deletion of either protein rendered the virus unviable. The

nonselective Ca^{2+} permeable ion channel accessory protein, open reading frame 3a (ORF 3a, 3a), has also been implicated in inflammasome activation and apoptosis for both SARS-CoV and SARS-CoV-2, however, its mechanistic understanding yet remains to be fully understood. The envelope (E) protein is a Ca^{2+} permeable channel that releases intracellular Ca^{2+} to trigger an increase of proinflammatory response, ultimately leading to cell death.

Viroporin, SARS-CoV E, protein is a small (~8-12 kDa) integral membrane protein for CoV assembly and budding. The E protein is mainly localized in in the ERGIC rather than the viral envelope itself, heavily implying its large role in the assembly of the viral envelope, though its exact role is not fully understood. One important aspect of the CoV E protein is its ability to self-assemble into protein-lipid pore allowing the transport of ions. Previous studies analyzing the ion specificity of the SARS-CoV E protein found preferential permeability to monovalent cations, Na^{+} and K^{+}, in reconstituted lipid bilayers [71, 74, 77]. However, E protein channel selectivity can be modulated to transport multivalent ions, Ca^{2+}, by interacting with the internal charges of their pores from the increased presence of negatively charged lipid head groups and acidic pH [71, 74, 77]. The E protein Ca^{2+} permeability can allow the virus to hijack the host cell's Ca^{2+} homeostasis machinery by: (1) quickly sequestering Ca^{2+}, maintaining low cytosolic Ca^{2+} levels to bypass immune responses from protein trafficking pathways for viral budding, and (2) exporting Ca^{2+}, drastically increasing cytosolic Ca^{2+} levels to signal the cell apoptotic pathway [71, 74, 77]. Additionally, it has been reported that the sudden efflux of Ca^{2+} from the E protein during viral entry triggers the overproduction

of IL-1ß, commonly linked to severe inflammatory diseases, such as the cytokine storm observed in patients diagnosed with COVID-19 [71, 74, 77].

ORF3a, a novel viral structural accessory protein, is composed of three transmembrane domains, forming an ion channel that heavily facilitates viral release and infection. 3a interacts with many structural proteins, such as S, M, and E protein [78]. The activity with S protein is rather interesting as it signifies the presence and role 3a has on viral assembly and release. This interaction occurs within the interior viral envelope with the formation of interchain disulfide bonds between cysteine-rich regions of the membrane-spanning domain and cytoplasmic tails; this is a well-conserved motif unique to the CoV S protein, now identified in 3a [79, 80]. Recent studies expanded on the multi-faceted role of 3a as the cytoplasmic tail was found to bind to calcium, resulting in a conformational change to reorient pre-existing helices, promoting the exposure of a hydrophobic cleft, a common property observed in Ca^{2+} sensor proteins [81]. Additionally, the presence of 3a during viral assembly increased the levels of intracellular vesicles, assisting in the nonlytic release of viral particles. 3a is also directly involved in the viral entry as SARS-CoV-2 3a was most recently observed to trigger cell death in cultured cells through the influx of Ca^{2+} as it activates apoptosis and contributes to the cytokine storm [76].

3.1.2.2. ENDO-LYSOSOMAL CALCIUM ION CHANNELS

Two-pore channels (TPCs) are NAADP-dependent Ca^{2+} ion channels, uniquely localized in acidic organelles, such as endosomes and lysosomes. TPCs are key for several functions - release of Ca^{2+} into the cytoplasm to help mediate biomolecule transport (i.e. receptor proteins and viruses) [75]. In the context of

viral entry, TPCs act as cellular indicators to signify where viral fusion occurs in the endosomal pathway with TPC1 in early endosome (biased endosomally) and TPC2 in late endosome (biased lysosomally) [75]. TPC silencing or blockers previously shown to significantly inhibit viral entry, most notably that of Ebolavirus (EBOV), MERS-CoV, and now SARS-CoV-2 [75]. For EBOV, the use of calcium channel blockers, specifically tetrandrine, were found inhibit NAADP-activating activity and TPC2 [69, 82]. Minimal is known on how exactly CCBs inhibit SARS-CoV-2 viral entry but performing similar studies on TPC2 SARS-CoV-2 viral entry could be a potential platform to rapidly detect the effectiveness on CCBs on viral entry.

3.1.3. PRELIMINARY WORK

3.1.3.1. L-TYPED CALCIUM CHANNEL BLOCKERS INHIBIT SARS-COV-2 ENTRY

Initial studies performed by Straus et al identified three promising CCBs to inhibit SARS-CoV infectivity for alternative therapeutics on COVID-19. This study utilized live SARS-CoV-2 and SARS2pp to study the inhibitory effect CCBs have as these viruses infect VeroE6 and Calu-3 cells, a lung epithelial cell. We performed a dose-response study by adding four different concentrations (10 μM, 50 μM, 100 μM, 500 μM) of each compound one-hour post infection. We also monitored cell viability under equivalent conditions. From the two viral platforms, we identified three drugs amlodipine, nifedipine, and felodipine to have the highest inhibitory effect on SARS-CoV, more specifically felodipine with a $TCID_{50}$ of 50 μM, approximately 80% cell

viability, and selectivity index of 9,784, showing high promise in its therapeutic efficacy in humans.

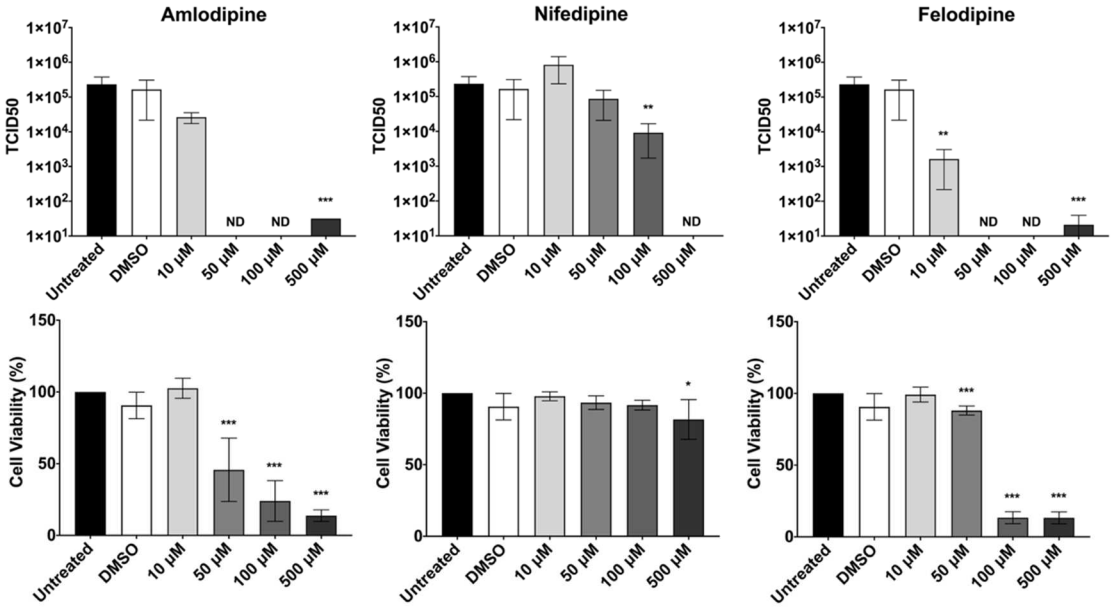

Figure 1. Inhibitory effect of three CCBs on live SARS-CoV-2 infection and correlation to cell viability in Calu-3 cells. *Infectivity***.** Calu-3 epithelial lung cells were infected with SARS-CoV-2 isolate USA-WA1/2020 at a MOI of 0.1 for 24 hours. The CCBS, amlodipine, nifedipine, and felodipine were added to the cells at the indicated concentrations immediately after the virus. 0 µM sample contained only DMSO which was used as a solvent for the drugs. TCID50s were performed with growth supernatants and calculated according to the Reed-Muench method. No bar means no virus was detected at the respective concentration. Error bars represent standard deviations (n = 3). *Cell viability*. Calu-3 epithelial lung cells were treated with the indicated concentrations of amlodipine, and nifedipine for 24 hours. After 24 hours, cell viability was measured using 3-(4,5-dimethylthiazol-2-yl)-2,5-diphenyltetrazolium bromide (MTT). Cell viability was determined by normalizing absorbance from the sample well by the average absorbance of untreated wells. As it was for the infections, 0 µM sample contained only DMSO which was used as solvent for the drugs. Asterisks indicate statistical significance compared to the untreated control. Statistical analysis was performed using an unpaired Student's t-test. * denotes $p < 0.05$, ** denotes $p < 0.01$, *** denotes $p < 0.001$.

3.1.4. SPECIFIC AIMS

3.1.4.1. AIM 1. VIROPORINS AS REGULATORY VIRION CA^{2+} SWITCHES FOR INCREASED SARS-COV-2 INFECTIVITY.

Considering our previous findings demonstrating the inhibitory effect CCBs has on live SARS-CoV-2 viruses and pseudoparticles, there is still a gap in understanding its exact mechanism of inhibition as we are limited by our pseudoparticle system, only being able to study viral entry from the perspective of the S protein. There are other structural proteins present within a viral particle, in addition to S protein, two of which are classified as viroporins, or ion channels. With that I hypothesize the presence of the viroporins in the viral membrane function as regulatory Ca^{2+} switches to evade regulatory pathways for nonlytic release and contribute to increased infectivity. To address this, Aim 1 will have two approaches: (1) observing Ca^{2+} flux during viral entry and release with the incorporation of E and 3a into the viral particle, and (2) study the protein-protein interactions (PPI) between S, 3a, and E upon Ca^{2+} binding.

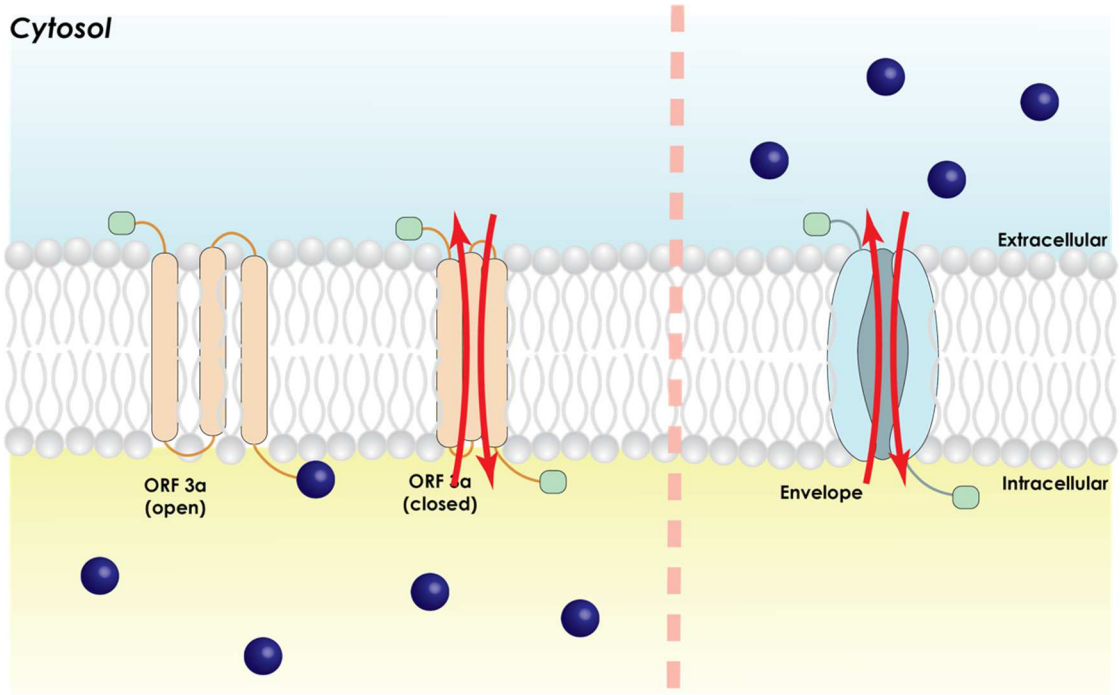

Figure 2. Study calcium dynamics in viroporins in vitro using Ca^{2+} signaling imaging methods. Viroporins, 3a and E, will encode a fluorescence Ca^{2+} indicator to track the flow of intracellular calcium to study effect calcium has on the viral ion channels in regards to the viral cycle.

To study the flow of Ca^{2+} within the viral particle, I will first tune the complexity of our MLV pseudoparticle system, established in the Whittaker lab, to incorporate 3a and E. I will utilize two platforms, MLVpp and VSVpp; both of which can provide infectivity measurements through two different methods, flow cytometry and luciferase luminescence, however VLPs contain a GFP reporter to allow single virion tracking for in vitro Ca^{2+} signaling imaging. By individually expressing 3a and E with the S protein, we will be able to assess changes in pseudoparticle infectivity and discern if the presence of viroporins increases infectivity. Upon which, we will chelate extracellular and intracellular Ca^{2+} with EGTA and BAPTA-AM, respectively, in the pseudoparticles to determine if Ca^{2+} affects the functionality of the viroporins during viral entry.

If there was an observed impact of Ca^{2+} on 3a or E infectivity, I will explore the movement of Ca^{2+} through Ca^{2+} signaling imaging methods. To do so, I plan to incorporate GCamp6, a genetically encoded Ca^{2+} indicator (GECI), onto the cytoplasmic tail of 3a and intracellular portion of E to study the kinetics of Ca^{2+} kinetics from binding to 3a and flow through E and express the recombinant proteins in HEK293T cells. Using confocal microscopy, I will identify the localization of the proteins using an ER and ERGIC tracker, ER-Tracker signaling. I will then use a Ca^{2+} ionophore, ionomycin, to deplete the fura-labeled Ca^{2+} stores sequestered from E and 3a, separately, to study changes in $[Ca^{2+}]$ in the cytosol. Following which, I will treat the cells with CCBs to observe any effect on the flow of Ca^{2+} from E and 3a. This will confirm the "switch" ability of the viroporins regarding viral assembly and release to

maintain appropriate [Ca^{2+}] levels to evade the post-translational regulatory pathways. Additionally, this opens the possibility of these viroporins as targets of CCBs.

To study the protein-protein interaction (PPI) between S, 3a, and E upon Ca^{2+} binding, I will utilize biophysical characterization techniques, isothermal calorimetry (ITC) and circular dichroism (CD), to not only study protein-protein binding, but also protein-Ca^{2+} binding. Prior studies identified a binding pocket within ORF3a that induces a conformational change that may better stabilize its binding with S, thereby promoting viral viability. This interaction occurs between the cytoplasmic tails of 3a and S, so by isolating the junctions of the transmembrane domain (TMD) and cytoplasmic tail of 3a and S we can observe each subunit's binding affinity to Ca^{2+} and changes in alpha helical structure. We will follow up by testing changes in S-3a binding upon Ca^{2+} binding leads to increased alpha helical content. These characterization techniques will give us an initial understanding on the role Ca^{2+} plays to increase the protein-protein interaction.

Based on our initial findings, I will develop a biomimetic platform to test the full protein-protein interaction under the presence of Ca^{2+} by detecting changes in membrane resistance using electrical impedance spectroscopy (EIS). Our group has demonstrated success in the use of conducting polymers, poly(3,4-ethylenedioxythiophene) polystyrene sulfonate (PEDOT:PSS), as support for supported lipid bilayer (SLB) formation for biosensing purposes. To study the ion channel activity of 3a and E, and protein-protein interaction of S and E under the presence of Ca^{2+}, will utilize HEK293T cells to express 3a, S, and E. Through the process of cell blebbing, I will form vesicles encapsulating these proteins and confirm their presence using

Western Blot analysis. To ensure uniform bilayer formation, the blebs will be characterized through Nanosight to determine its size and concentration.

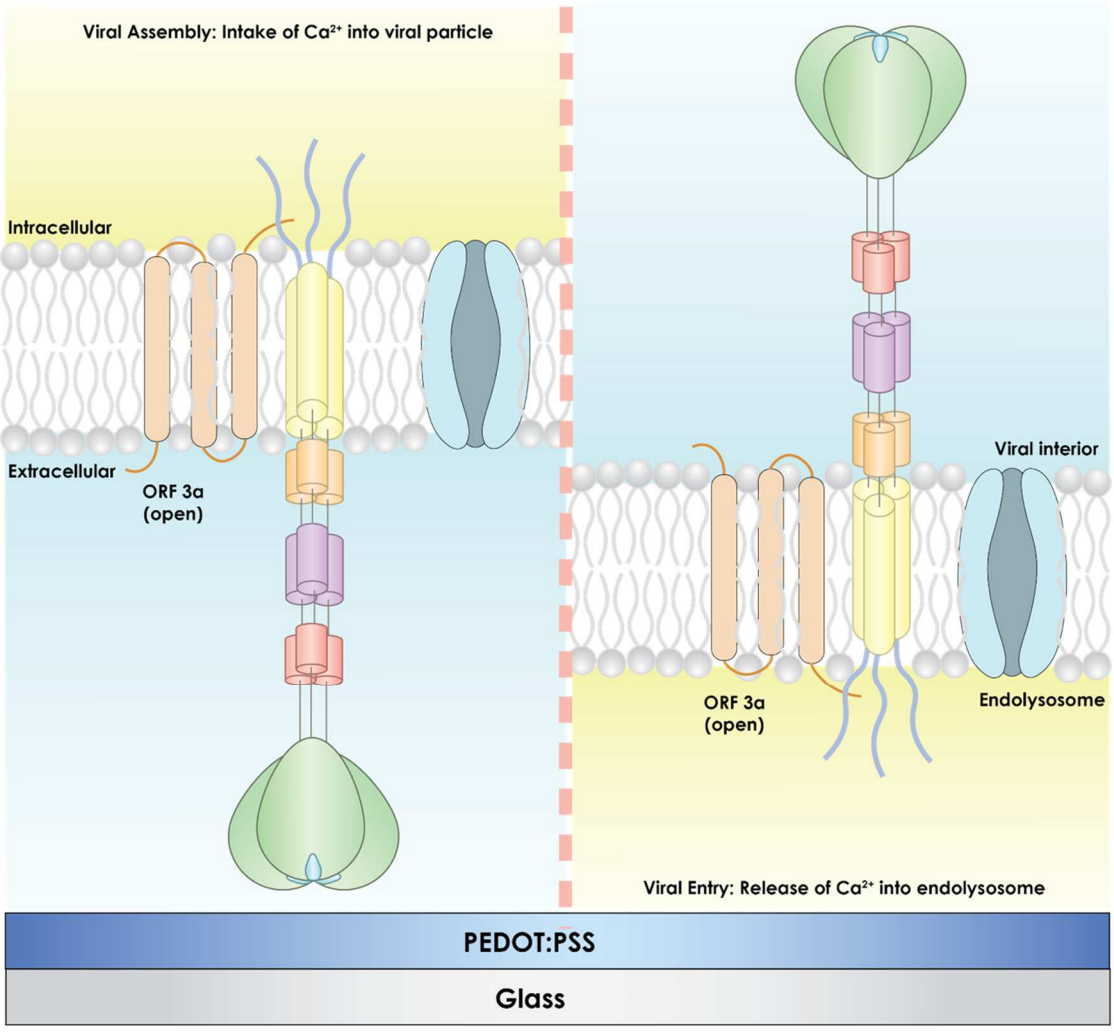

Figure 3. Development of a biomimetic platform to study the protein-protein interaction between viroporins. This is a proposed interaction between the three viroporins: 3a, S, and E. This biomimetic platform will allow optoelectronic measurements to study the changes in membrane rigidity induced by the three viroporins working in conjunction under the presence of calcium to imitate viral assembly/budding and entry.

The challenge for developing this platform regarding ion channels, such as E, the electrical measurements are restricted to the influx of Ca^{2+}. For the case of 3a, Ca^{2+} binding occurs in the interior portion of the bilayer. To address this, I will utilize a

recently published method from Lyu *et al* employing a blotting method on a supported bilayer to study the cytoplasmic side of the membrane protein. To assess bilayer quality after the blotting method, fluorescence recovery after photobleaching (FRAP) will be used to determine the mobility and diffusivity of the bilayer. The correct bilayer orientation will then be confirmed using total internal fluorescence microscopy (TIRF-M) with mAb binding, specifically binding to the cytoplasmic side of the proteins, such as the S2 subunit of S protein. To evaluate the impact of Ca2+ binding on further stabilizing S-3a protein interaction, I will observe the changes in membrane resistances with EIS as I add a calcium chelator, EGTA, in a concentration dependent manner to assess if the removal of Ca^{2+} will regain membrane mobility. I will then evaluate changes if CCBs bind to the 3a-S complex and E affect the membrane resistance. This biomimetic platform will not only inform us on the impact Ca^{2+} binding/flow has on membrane properties, but also provide more insight on the stability of the S protein during viral entry due to PPI with 3a and E under Ca^{2+}-rich conditions.

Recent studies identified a unique motif within the CoV S protein to catalyze the ESCRT (endosomal sorting complexes required for transport) pathway to facilitate membrane fission and viral budding for many enveloped viruses. Additionally, the E protein is capable of alternating membrane curvature, like that of influenza M2 protein. Traditional methods of observing viral assembly and release require the use of electron microscopy, however, as an alternative, I will utilize a system to image and monitor membrane budding within giant unilamellar vesicles (GUVs) previously described for analyzing the function of proteins in the ESCRT complex. With this system, we will be able to better observe the binding order of the structural proteins, in addition to visualize

the impact Ca^{2+} has on E and 3a to assist in viral budding. For these tests, we will be utilizing purified S, E, and 3a proteins.

To address the role of 3a and E in virus budding, we will first assess the effect each protein has on membrane curvature by reconstituting each protein in a large unilamellar vesicles (LUVs). As E also functions as an ion channel and is responsible for membrane budding, we will also address the possibility of Ca^{2+} dependent alterations in membrane curvature by the E protein. Using GUVs, we can evaluate the protein-protein interaction of S, E, and 3a during membrane scission under Ca^{2+} conditions, if it was found to play a role in membrane curvature. We will test different sequential combinations of protein reconstitution to determine the order in which the vesicle will bud off with all the proteins. By observing the Ca^{2+} E-induced budding, we can test the impact Ca^{2+} chelators, BAPTA-AM or EGTA, have on inhibiting membrane budding, where we follow up this study using CCBs to determine if it can impact membrane budding mediated from viroporins.

3.1.4.2. AIM 2. DEVELOPMENT OF A BIOSENSING PLATFORM TO RAPIDLY DETECT THE EFFECTIVENESS OF $_{L}$-TYPE CALCIUM CHANNEL BLOCKERS ON TPC2

TPC2 not only has a major role in endosome maturation, but also helps mitigate viral entry, specifically for MERS-CoV and SARS-CoV-2. As more highly infectious variants arise, there is an increasing need for alternative therapeutics to mitigate CoV infection. Due to the role calcium has in promoting CoV membrane fusion, initial studies focusing on the inhibitory effect FDA-approved $_{L}$-type calcium channel blockers have identified three promising therapeutics. However, the Ca^{2+} target for these CCBs, in the context of SARS-CoV-2, is not very understood. To gain a better understanding

on the inhibitory mechanism of CCBs, I plan on studying TPC2 as the target ion channel through two approaches: (1) study the flow of Ca^{2+} in TPC2 within a biological system using calcium signaling methods and (2) develop a biosensing platform, well-established in the Daniel lab, to rapidly detect the effect CCBs have on the Ca^{2+} influx in TPC2.

To better understand the impact TPC2 has on SARS-CoV-2 entry through the endosomal pathway, I will perform colocalization infection experiments to visually track the movement of the virus within VeroE6 cells. For these studies, I will utilize the VLP platform that contains a GFP tag in the pseudoparticle, TPC2 with an mCherry tag, Lysotracker to track the movement of the lysosome prior to membrane fusion and confirm that SARS-CoV-2 membrane fusion occurs in acidic endosomes by tagging lysosomal associated membrane protein 1 (LAMP1). To confirm the importance of TPC2 on SARS-CoV-2 entry, I will treat VeroE6 cells with TPC2-specific siRNAs to observe changes in infectivity and potential inhibition of viral trafficking in endosomal compartments. For both conditions, I will also then track the changes in Ca^{2+} homeostasis using Fluo-4, a high-affinity Ca^{2+} dye, to observe a rise in endosomal Ca^{2+} triggers the activity of TPC2 as it progresses endosomal maturation to mediate viral entry. Once we determine the role of TPC2 in viral entry, we will assess if the CCBs from prior studies (amlodipine, nifedipine, and felodipine) inhibit TPC2 function by investigating how the CCB affects the colocalization of SARS-CoV-2 VLPs with TPC-positive endosomes. By measuring how CCBs affect both the Ca^{2+} flux and TPC2 function, we gain a more mechanistic understanding on the inhibitory mechanism has on SARS-CoV-2 endosomal entry.

As TPC2 is confirmed to have an integral role in SARS-CoV-2 viral entry, there is an increasing need to rapidly identify effective therapeutics to block TPC2 function. For the past few years, the Daniel lab has worked on developing a bio sensing platform composed of support lipid bilayers on conducting polymers, mimicking the in vitro cellular environment to better study the activity of membrane proteins, such as ion channels, by detecting subtle changes in membrane properties using EIS and organic electrochemical transistors (OECT). By building off on the platform developed in Aim 1 to study the IC activity of viroporins, E and 3a, we can better distinguish more effective therapeutics on TPC2. As TPC2 naturally resides in lysosomal compartments, I will isolate and purify lysosomes from VeroE6 cells. To identify the isolated lysosomes, acid phosphatase will be used as a marker as it normally resides in lysosomes and Western Blot analysis will further characterize the lysosomes by using antibodies to detect the presence of LAMP1, a lysosome specific marker, and TPC2. To ensure the purity of the lysosomes, we will examine the possibility of plasma membrane contamination by probing the presence of plasma membrane protein, caveolin. Additionally, for further lysosomal characterization, I will use Nanosight to quantify its size and concentration. As TPC2 requires NAADP to activate Ca^{2+} flow through the channel, we have to devise an OECT platform that permits the flow of NAADP between PEDOT:PSS and the bilayer. To do so, we will deposit PEDOT:PSS on glass, place a PDMS well that holds a transwell containing a semipermeable membrane to contain the lysosomal bilayer and to allow the flow of NAADP in between the PEDOT:PSS and transwell to stimulate TPC2 channel activity. To ensure no leakage of the lysosomal bilayer, we will fluorescently label the lysosomes with R18 and use point-scanning

confocal microscopy to assess the area and depth of the bilayer coverage in the transwell filter. I will further characterize the lysosome bilayers in the transwell using the techniques previously described in Aim 1.

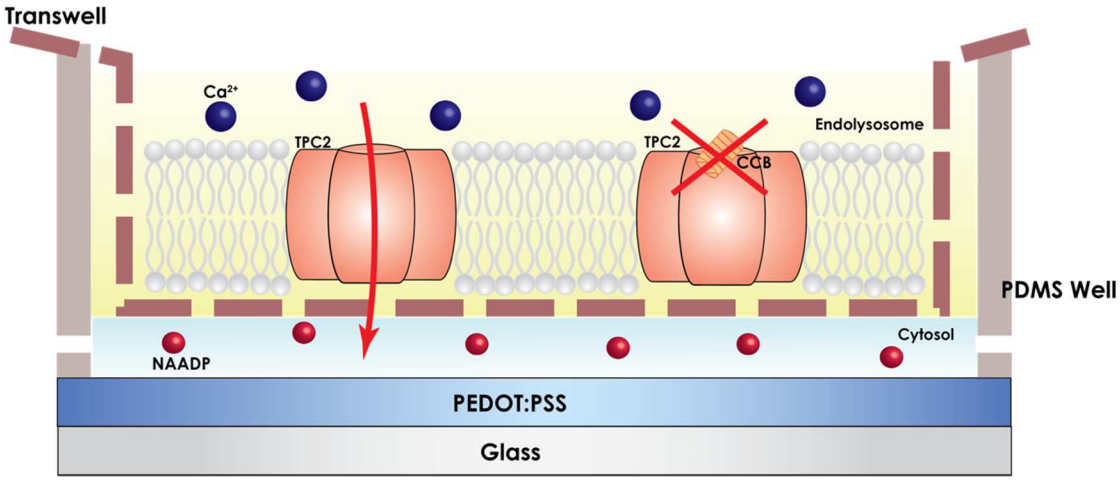

Figure 4. Rapid detection of calcium channel blockers on endolysosomal Ca2+ ion channel, TPC2. This is a novel biomimetic platform to simulate an in vivo environment to allow a more accurate study of ion channel behavior, such as TPC2.

To detect Ca^{2+} influx activity of TPC2, we will use EIS to assess initial membrane impedance of our system without NAADP as a baseline to signify the closed conformation of TPC2. We will then detect changes in the membrane as we add NAADP in a dose-dependent manner. Once we gain an understanding on the pore formation activity of TPC2 with the presence of NAADP, we will examine the effects of pH under constant presence of NAADP as acidic pH is required for a high [Ca^{2+}]. To distinguish which CCBs inhibit TPC2 activity, we can utilize TPC2 agonist, TPC2-A1-P to induce increased Ca^{2+} responses from TPC2, a function that can be blocked specifically by TPC2 blockers. Based on this, we can identify which CCB can target TPC2 as we hypothesize the presence of CCBs will block the increased flux of Ca^{2+}, thereby closing the ion channel as signaled by decreased membrane impedance.

3.1.5. CONCLUSION

Recent studies from Daniel and Whittaker labs identified certain CCBs to inhibit SARS-CoV-2 infections as possible treatments of COVID-19 using live SARS-CoV-2 virus and SARS-CoV-2pp. The exact mechanism of inhibition needs to be address as there are discrepancies between the two platforms, live virus and pseudotyped virus, that are not addressed, namely with the pseudoparticle system as we are limited to studies on viral entry mediated by the S protein. Broadening our understanding on the impact Ca^{2+} has on the CoV life cycle, by the effect of Ca^{2+} ion channels (*i.e.* 3a, E, TPC2) on viral assembly/release and entry, will provide us more mechanistic insight on how CCBs can impede viral infection.

CHAPTER 4
REFERENCES

1. Tang T, Bidon M, Jaimes JA, Whittaker GR, Daniel S. Coronavirus membrane fusion mechanism offers a potential target for antiviral development. Antiviral Res. 2020;178:104792. Epub 2020/04/10. doi: 10.1016/j.antiviral.2020.104792. PubMed PMID: 32272173; PubMed Central PMCID: PMCPMC7194977.
2. Dubé M, Rey FA, Kielian M. Rubella Virus: First Calcium-Requiring Viral Fusion Protein. PLOS Pathogens. 2014;10(12):e1004530. doi: 10.1371/journal.ppat.1004530.
3. Nathan L, Lai AL, Millet JK, Straus MR, Freed JH, Whittaker GR, et al. Calcium Ions Directly Interact with the Ebola Virus Fusion Peptide To Promote Structure-Function Changes That Enhance Infection. ACS Infect Dis. 2020;6(2):250-60. Epub 2019/11/21. doi: 10.1021/acsinfecdis.9b00296. PubMed PMID: 31746195; PubMed Central PMCID: PMCPMC7040957.
4. Crespi B, Alcock J. Conflicts over calcium and the treatment of COVID-19. Evolution, Medicine, and Public Health. 2021;9(1):149-56. doi: 10.1093/emph/eoaa046.
5. Danta CC. Calcium Channel Blockers: A Possible Potential Therapeutic Strategy for the Treatment of Alzheimer's Dementia Patients with SARS-CoV-2 Infection. ACS Chemical Neuroscience. 2020;11(15):2145-8. doi: 10.1021/acschemneuro.0c00391.
6. Lai AL, Millet JK, Daniel S, Freed JH, Whittaker GR. The SARS-CoV Fusion Peptide Forms an Extended Bipartite Fusion Platform that Perturbs Membrane Order in a Calcium-Dependent Manner. J Mol Biol. 2017;429(24):3875-92. Epub 2017/10/24. doi: 10.1016/j.jmb.2017.10.017. PubMed PMID: 29056462; PubMed Central PMCID: PMCPMC5705393.
7. Belouzard S, Chu VC, Whittaker GR. Activation of the SARS coronavirus spike protein via sequential proteolytic cleavage at two distinct sites. Proceedings of the National Academy of Sciences. 2009;106(14):5871. doi: 10.1073/pnas.0809524106.
8. Bosch BJ, van der Zee R, de Haan CA, Rottier PJ. The coronavirus spike protein is a class I virus fusion protein: structural and functional characterization of the fusion core complex. J Virol. 2003;77(16):8801-11. Epub 2003/07/30. doi: 10.1128/jvi.77.16.8801-8811.2003. PubMed PMID: 12885899; PubMed Central PMCID: PMCPMC167208.
9. de Haan CAM, Rottier PJM. Molecular Interactions in the Assembly of Coronaviruses. Advances in Virus Research. 64: Academic Press; 2005. p. 165-230.
10. Millet JK, Whittaker GR. Host cell proteases: Critical determinants of coronavirus tropism and pathogenesis. Virus Res. 2015;202:120-34. Epub 2014/12/03. doi: 10.1016/j.virusres.2014.11.021. PubMed PMID: 25445340; PubMed Central PMCID: PMCPMC4465284.

11. Millet JK, Whittaker GR. Physiological and molecular triggers for SARS-CoV membrane fusion and entry into host cells. Virology. 2018;517:3-8. Epub 2017/12/26. doi: 10.1016/j.virol.2017.12.015. PubMed PMID: 29275820.
12. Li W, Moore MJ, Vasilieva N, Sui J, Wong SK, Berne MA, et al. Angiotensin-converting enzyme 2 is a functional receptor for the SARS coronavirus. Nature. 2003;426(6965):450-4. doi: 10.1038/nature02145.
13. Zhou P, Yang XL, Wang XG, Hu B, Zhang L, Zhang W, et al. A pneumonia outbreak associated with a new coronavirus of probable bat origin. Nature. 2020;579(7798):270-3. Epub 2020/02/06. doi: 10.1038/s41586-020-2012-7. PubMed PMID: 32015507; PubMed Central PMCID: PMCPMC7095418.
14. White JM, Whittaker GR. Fusion of Enveloped Viruses in Endosomes. Traffic. 2016;17(6):593-614. Epub 2016/03/05. doi: 10.1111/tra.12389. PubMed PMID: 26935856; PubMed Central PMCID: PMCPMC4866878.
15. Park JE, Li K, Barlan A, Fehr AR, Perlman S, McCray PB, Jr., et al. Proteolytic processing of Middle East respiratory syndrome coronavirus spikes expands virus tropism. Proc Natl Acad Sci U S A. 2016;113(43):12262-7. Epub 2016/10/30. doi: 10.1073/pnas.1608147113. PubMed PMID: 27791014; PubMed Central PMCID: PMCPMC5086990.
16. Simmons G, Bertram S, Glowacka I, Steffen I, Chaipan C, Agudelo J, et al. Different host cell proteases activate the SARS-coronavirus spike-protein for cell-cell and virus-cell fusion. Virology. 2011;413(2):265-74. Epub 2011/03/26. doi: 10.1016/j.virol.2011.02.020. PubMed PMID: 21435673; PubMed Central PMCID: PMCPMC3086175.
17. Simmons G, Zmora P, Gierer S, Heurich A, Pohlmann S. Proteolytic activation of the SARS-coronavirus spike protein: cutting enzymes at the cutting edge of antiviral research. Antiviral Res. 2013;100(3):605-14. Epub 2013/10/15. doi: 10.1016/j.antiviral.2013.09.028. PubMed PMID: 24121034; PubMed Central PMCID: PMCPMC3889862.
18. Matsuyama S, Nagata N, Shirato K, Kawase M, Takeda M, Taguchi F. Efficient Activation of the Severe Acute Respiratory Syndrome Coronavirus Spike Protein by the Transmembrane Protease TMPRSS2. Journal of Virology. 2010;84(24):12658-64. doi: 10.1128/JVI.01542-10.
19. Glowacka I, Bertram S, Müller Marcel A, Allen P, Soilleux E, Pfefferle S, et al. Evidence that TMPRSS2 Activates the Severe Acute Respiratory Syndrome Coronavirus Spike Protein for Membrane Fusion and Reduces Viral Control by the Humoral Immune Response. Journal of Virology. 2011;85(9):4122-34. doi: 10.1128/JVI.02232-10.
20. Hoffmann M, Kleine-Weber H, Schroeder S, Krüger N, Herrler T, Erichsen S, et al. SARS-CoV-2 Cell Entry Depends on ACE2 and TMPRSS2 and Is Blocked by a Clinically Proven Protease Inhibitor. Cell. 2020;181(2):271.
21. Matsuyama S, Nao N, Shirato K, Kawase M, Saito S, Takayama I, et al. Enhanced isolation of SARS-CoV-2 by TMPRSS2-expressing cells. Proceedings of the National Academy of Sciences. 2020;117(13):7001. doi: 10.1073/pnas.2002589117.

22. Jaimes JA, Millet JK, Whittaker GR. Proteolytic Cleavage of the SARS-CoV-2 Spike Protein and the Role of the Novel S1/S2 Site. iScience. 2020;23(6):101212. doi: https://doi.org/10.1016/j.isci.2020.101212.
23. Tang T, Jaimes JA, Bidon MK, Straus MR, Daniel S, Whittaker GR. Proteolytic Activation of SARS-CoV-2 Spike at the S1/S2 Boundary: Potential Role of Proteases beyond Furin. ACS Infect Dis. 2021;7(2):264-72. Epub 2021/01/13. doi: 10.1021/acsinfecdis.0c00701. PubMed PMID: 33432808; PubMed Central PMCID: PMCPMC7839419.
24. Wang H, Yang P, Liu K, Guo F, Zhang Y, Zhang G, et al. SARS coronavirus entry into host cells through a novel clathrin- and caveolae-independent endocytic pathway. Cell Res. 2008;18(2):290-301. Epub 2008/01/30. doi: 10.1038/cr.2008.15. PubMed PMID: 18227861; PubMed Central PMCID: PMCPMC7091891.
25. Ou X, Liu Y, Lei X, Li P, Mi D, Ren L, et al. Characterization of Spike Glycoprotein of SARS-CoV-2 on Virus Entry and Its Immune Cross-Reactivity with SARS-CoV. Nat Commun. 2020;11(1):1620.
26. Zhou Y, Frey TK, Yang JJ. Viral calciomics: Interplays between Ca2+ and virus. Cell Calcium. 2009;46(1):1-17. doi: https://doi.org/10.1016/j.ceca.2009.05.005.
27. Straus MR, Tang T, Lai AL, Flegel A, Bidon M, Freed JH, et al. Ca(2+) Ions Promote Fusion of Middle East Respiratory Syndrome Coronavirus with Host Cells and Increase Infectivity. J Virol. 2020;94(13). Epub 2020/04/17. doi: 10.1128/JVI.00426-20. PubMed PMID: 32295925; PubMed Central PMCID: PMCPMC7307142.
28. Lai AL, Freed JH. SARS-CoV-2 Fusion Peptide has a Greater Membrane Perturbating Effect than SARS-CoV with Highly Specific Dependence on Ca2+. Journal of Molecular Biology. 2021;433(10):166946. doi: https://doi.org/10.1016/j.jmb.2021.166946.
29. Khelashvili G, Plante A, Doktorova M, Weinstein H. Ca²⁺-dependent mechanism of membrane insertion and destabilization by the SARS-CoV-2 fusion peptide. Biophysical Journal. 2021;120(6):1105-19. doi: 10.1016/j.bpj.2021.02.023.
30. Lai MMC, Cavanagh D. The Molecular Biology of Coronaviruses. Elsevier; 1997. p. 1-100.
31. Masters PS. The Molecular Biology of Coronaviruses. Advances in Virus Research2006. p. 193-292.
32. Cherry JD, Krogstad P. SARS: the first pandemic of the 21st century. Pediatr Res. 2004;56(1):1-5. Epub 2004/05/21. doi: 10.1203/01.PDR.0000129184.87042.FC. PubMed PMID: 15152053; PubMed Central PMCID: PMCPMC7086556.
33. de Groot RJ, Baker SC, Baric RS, Brown CS, Drosten C, Enjuanes L, et al. Middle East respiratory syndrome coronavirus (MERS-CoV): announcement of the Coronavirus Study Group. J Virol. 2013;87(14):7790-2. Epub 2013/05/17. doi: 10.1128/JVI.01244-13. PubMed PMID: 23678167; PubMed Central PMCID: PMCPMC3700179.
34. Wu F, Zhao S, Yu B, Chen YM, Wang W, Song ZG, et al. A new coronavirus associated with human respiratory disease in China. Nature. 2020;579(7798):265-9. Epub 2020/02/06. doi: 10.1038/s41586-020-2008-3. PubMed PMID: 32015508; PubMed Central PMCID: PMCPMC7094943.

35. M SM, P M, F A-S, C R, MP K, B M. World Health Organization methodology to prioritize emerging infectious diseases in need of research and development. Emerg Infect Dis. 2018. doi: 10.3201/eid2409.171427.
36. da Costa VG, Moreli ML, Saivish MV. The emergence of SARS, MERS and novel SARS-2 coronaviruses in the 21st century. Arch Virol. 2020;165(7):1517-26. Epub 2020/04/22. doi: 10.1007/s00705-020-04628-0. PubMed PMID: 32322993.
37. Velavan TP, Meyer CG. The COVID-19 epidemic. Trop Med Int Health. 2020;25(3):278-80. Epub 2020/02/16. doi: 10.1111/tmi.13383. PubMed PMID: 32052514.
38. de Wit E, van Doremalen N, Falzarano D, Munster VJ. SARS and MERS: recent insights into emerging coronaviruses. Nat Rev Microbiol. 2016;14(8):523-34. Epub 2016/06/28. doi: 10.1038/nrmicro.2016.81. PubMed PMID: 27344959.
39. Belouzard S, Millet JK, Licitra BN, Whittaker GR. Mechanisms of coronavirus cell entry mediated by the viral spike protein. Viruses. 2012;4(6):1011-33. Epub 2012/07/21. doi: 10.3390/v4061011. PubMed PMID: 22816037; PubMed Central PMCID: PMCPMC3397359.
40. Lee C-Y, Lowen AC. Animal models for SARS-CoV-2. Current Opinion in Virology. 2021;48:73-81. doi: 10.1016/j.coviro.2021.03.009.
41. Stevens CS, Oguntuyo KY, Benhur L. Proteases and variants: context matters for SARS-CoV-2 entry assays. Current Opinion in Virology. 2021. doi: 10.1016/j.coviro.2021.07.004.
42. Madu IG, Roth SL, Belouzard S, Whittaker GR. Characterization of a highly conserved domain within the severe acute respiratory syndrome coronavirus spike protein S2 domain with characteristics of a viral fusion peptide. J Virol. 2009;83(15):7411-21. Epub 2009/05/15. doi: 10.1128/JVI.00079-09. PubMed PMID: 19439480; PubMed Central PMCID: PMCPMC2708636.
43. Basso LG, Vicente EF, Crusca E, Jr., Cilli EM, Costa-Filho AJ. SARS-CoV fusion peptides induce membrane surface ordering and curvature. Sci Rep. 2016;6:37131. Epub 2016/11/29. doi: 10.1038/srep37131. PubMed PMID: 27892522; PubMed Central PMCID: PMCPMC5125003.
44. Koppisetti RK, Fulcher YG, Van Doren SR. Fusion Peptide of SARS-CoV-2 Spike Rearranges into a Wedge Inserted in Bilayered Micelles. Journal of the American Chemical Society. 2021. doi: 10.1021/jacs.1c05435.
45. Millet JK, Tang T, Nathan L, Jaimes JA, Hsu HL, Daniel S, et al. Production of Pseudotyped Particles to Study Highly Pathogenic Coronaviruses in a Biosafety Level 2 Setting. J Vis Exp. 2019;(145). Epub 2019/03/19. doi: 10.3791/59010. PubMed PMID: 30882796.
46. Olsson MHM, Søndergaard CR, Rostkowski M, Jensen JH. PROPKA3: Consistent Treatment of Internal and Surface Residues in Empirical pKa Predictions. Journal of Chemical Theory and Computation. 2011;7(2):525-37. doi: 10.1021/ct100578z.
47. Humphrey W, Dalke A, Schulten K. VMD: Visual molecular dynamics. Journal of Molecular Graphics. 1996;14(1):33-8. doi: https://doi.org/10.1016/0263-7855(96)00018-5.

48. Phillips JC, Braun R, Wang W, Gumbart J, Tajkhorshid E, Villa E, et al. Scalable molecular dynamics with NAMD. Journal of Computational Chemistry. 2005;26(16):1781-802. doi: https://doi.org/10.1002/jcc.20289.
49. Essmann U, Perera L, Berkowitz ML, Darden T, Lee H, Pedersen LG. A smooth particle mesh Ewald method. The Journal of Chemical Physics. 1995;103(19):8577-93. doi: 10.1063/1.470117.
50. Evans DJ, Holian BL. The Nose–Hoover thermostat. The Journal of Chemical Physics. 1985;83(8):4069-74. doi: 10.1063/1.449071.
51. Eastman P, Swails J, Chodera JD, McGibbon RT, Zhao Y, Beauchamp KA, et al. OpenMM 7: Rapid development of high performance algorithms for molecular dynamics. PLOS Computational Biology. 2017;13(7):e1005659. doi: 10.1371/journal.pcbi.1005659.
52. Huang J, Rauscher S, Nawrocki G, Ran T, Feig M, de Groot BL, et al. CHARMM36m: an improved force field for folded and intrinsically disordered proteins. Nature Methods. 2017;14(1):71-3. doi: 10.1038/nmeth.4067.
53. Venable RM, Luo Y, Gawrisch K, Roux B, Pastor RW. Simulations of Anionic Lipid Membranes: Development of Interaction-Specific Ion Parameters and Validation Using NMR Data. The Journal of Physical Chemistry B. 2013;117(35):10183-92. doi: 10.1021/jp401512z.
54. Gui M, Song W, Zhou H, Xu J, Chen S, Xiang Y, et al. Cryo-electron microscopy structures of the SARS-CoV spike glycoprotein reveal a prerequisite conformational state for receptor binding. Cell Res. 2017;27(1):119-29. Epub 2016/12/23. doi: 10.1038/cr.2016.152. PubMed PMID: 28008928; PubMed Central PMCID: PMCPMC5223232.
55. Cheung G, Cousin MA. Synaptic Vesicle Generation from Activity-Dependent Bulk Endosomes Requires Calcium and Calcineurin. The Journal of Neuroscience. 2013;33(8):3370. doi: 10.1523/JNEUROSCI.4697-12.2013.
56. Tsien RY. A non-disruptive technique for loading calcium buffers and indicators into cells. Nature. 1981;290(5806):527-8. doi: 10.1038/290527a0.
57. Tang Q, Jin M-W, Xiang J-Z, Dong M-Q, Sun H-Y, Lau C-P, et al. The membrane permeable calcium chelator BAPTA-AM directly blocks human ether a-go-go-related gene potassium channels stably expressed in HEK 293 cells. Biochemical Pharmacology. 2007;74(11):1596-607. doi: https://doi.org/10.1016/j.bcp.2007.07.042.
58. Madu IG, Belouzard S, Whittaker GR. SARS-coronavirus spike S2 domain flanked by cysteine residues C822 and C833 is important for activation of membrane fusion. Virology. 2009;393(2):265-71. Epub 2009/09/01. doi: 10.1016/j.virol.2009.07.038. PubMed PMID: 19717178; PubMed Central PMCID: PMCPMC3594805.
59. Du L, He Y, Zhou Y, Liu S, Zheng BJ, Jiang S. The spike protein of SARS-CoV--a target for vaccine and therapeutic development. Nat Rev Microbiol. 2009;7(3):226-36. Epub 2009/02/10. doi: 10.1038/nrmicro2090. PubMed PMID: 19198616; PubMed Central PMCID: PMCPMC2750777.
60. Lu G, Wang Q, Gao GF. Bat-to-human: spike features determining 'host jump' of coronaviruses SARS-CoV, MERS-CoV, and beyond. Trends Microbiol.

2015;23(8):468-78. Epub 2015/07/25. doi: 10.1016/j.tim.2015.06.003. PubMed PMID: 26206723.
61. Schaefer SL, Jung H, Hummer G. Binding of SARS-CoV-2 Fusion Peptide to Host Endosome and Plasma Membrane. The Journal of Physical Chemistry B. 2021;125(28):7732-41. doi: 10.1021/acs.jpcb.1c04176.
62. Cai Y, Zhang J, Xiao T, Peng H, Sterling SM, Walsh RM, et al. Distinct conformational states of SARS-CoV-2 spike protein. Science. 2020;369(6511):1586. doi: 10.1126/science.abd4251.
63. Straus MR, Bidon M, Tang T, Whittaker GR, Daniel S. FDA approved calcium channel blockers inhibit SARS-CoV-2 infectivity in epithelial lung cells. bioRxiv. 2020:2020.07.21.214577. doi: 10.1101/2020.07.21.214577.
64. Danta CC. Calcium Channel Blockers: A Possible Potential Therapeutic Strategy for the Treatment of Alzheimer's Dementia Patients with SARS-CoV-2 Infection. ACS Chem Neurosci. 2020;11(15):2145-8. Epub 2020/07/15. doi: 10.1021/acschemneuro.0c00391. PubMed PMID: 32662982.
65. Borges V, Isidro J, Cortes-Martins H, Duarte S, Vieira L, Leite R, et al. Massive dissemination of a SARS-CoV-2 Spike Y839 variant in Portugal. Emerging Microbes & Infections. 2020;9(1):2488-96. doi: 10.1080/22221751.2020.1844552.
66. Korber B, Fischer WM, Gnanakaran S, Yoon H, Theiler J, Abfalterer W, et al. Tracking Changes in SARS-CoV-2 Spike: Evidence that D614G Increases Infectivity of the COVID-19 Virus. Cell. 2020;182(4):812-27.e19. doi: https://doi.org/10.1016/j.cell.2020.06.043.
67. Li Q, Wu J, Nie J, Zhang L, Hao H, Liu S, et al. The Impact of Mutations in SARS-CoV-2 Spike on Viral Infectivity and Antigenicity. Cell. 2020;182(5):1284-94.e9. doi: https://doi.org/10.1016/j.cell.2020.07.012.
68. Zhang L-K, Sun Y, Zeng H, Wang Q, Jiang X, Shang W-J, et al. Calcium channel blocker amlodipine besylate therapy is associated with reduced case fatality rate of COVID-19 patients with hypertension. Cell Discovery. 2020;6(1):96. doi: 10.1038/s41421-020-00235-0.
69. Gregory SM, Harada E, Liang B, Delos SE, White JM, Tamm LK. Structure and Function of the Complete Internal Fusion Loop from Ebolavirus Glycoprotein 2. Proc Natl Acad Sci U S A. 2011;108(27):11211.
70. Zhou Y, Xue S, Yang JJ. Calciomics: integrative studies of Ca2+-binding proteins and their interactomes in biological systems†. Metallomics. 2013;5(1):29-42. doi: 10.1039/c2mt20009k.
71. Verdiá-Báguena C, Nieto-Torres JL, Alcaraz A, DeDiego ML, Torres J, Aguilella VM, et al. Coronavirus E protein forms ion channels with functionally and structurally-involved membrane lipids. Virology. 2012;432(2):485-94. doi: https://doi.org/10.1016/j.virol.2012.07.005.
72. Wilson L, McKinlay C, Gage P, Ewart G. SARS coronavirus E protein forms cation-selective ion channels. Virology. 2004;330(1):322-31. doi: https://doi.org/10.1016/j.virol.2004.09.033.
73. Castaño-Rodriguez C, Honrubia Jose M, Gutiérrez-Álvarez J, DeDiego Marta L, Nieto-Torres Jose L, Jimenez-Guardeño Jose M, et al. Role of Severe Acute

Respiratory Syndrome Coronavirus Viroporins E, 3a, and 8a in Replication and Pathogenesis. mBio. 9(3):e02325-17. doi: 10.1128/mBio.02325-17.
74. Cabrera-Garcia D, Bekdash R, Abbott GW, Yazawa M, Harrison NL. The envelope protein of SARS-CoV-2 increases intra-Golgi pH and forms a cation channel that is regulated by pH. The Journal of Physiology. 2021;599(11):2851-68. doi: https://doi.org/10.1113/JP281037.
75. Zhao Z, Qin P, Huang Y-W. Lysosomal ion channels involved in cellular entry and uncoating of enveloped viruses: Implications for therapeutic strategies against SARS-CoV-2. Cell calcium. 2021;94:102360-. Epub 2021/01/23. doi: 10.1016/j.ceca.2021.102360. PubMed PMID: 33516131.
76. Kern DM, Sorum B, Mali SS, Hoel CM, Sridharan S, Remis JP, et al. Cryo-EM structure of SARS-CoV-2 ORF3a in lipid nanodiscs. Nature Structural & Molecular Biology. 2021;28(7):573-82. doi: 10.1038/s41594-021-00619-0.
77. Verdiá-Báguena C, Nieto-Torres JL, Alcaraz A, DeDiego ML, Enjuanes L, Aguilella VM. Analysis of SARS-CoV E protein ion channel activity by tuning the protein and lipid charge. Biochimica et Biophysica Acta (BBA) - Biomembranes. 2013;1828(9):2026-31. doi: https://doi.org/10.1016/j.bbamem.2013.05.008.
78. Sharma K, Surjit M, Satija N, Liu B, Chow VTK, Lal SK. The 3a Accessory Protein of SARS Coronavirus Specifically Interacts with the 5'UTR of Its Genomic RNA, Using a Unique 75 Amino Acid Interaction Domain. Biochemistry. 2007;46(22):6488-99. doi: 10.1021/bi062057p.
79. Zeng R, Yang R-F, Shi M-D, Jiang M-R, Xie Y-H, Ruan H-Q, et al. Characterization of the 3a protein of SARS-associated coronavirus in infected vero E6 cells and SARS patients. Journal of molecular biology. 2004;341(1):271-9. doi: 10.1016/j.jmb.2004.06.016. PubMed PMID: 15312778.
80. Liu DX, Fung TS, Chong KK-L, Shukla A, Hilgenfeld R. Accessory proteins of SARS-CoV and other coronaviruses. Antiviral Research. 2014;109:97-109. doi: https://doi.org/10.1016/j.antiviral.2014.06.013.
81. Minakshi R, Padhan K, Rehman S, Hassan MI, Ahmad F. The SARS Coronavirus 3a protein binds calcium in its cytoplasmic domain. Virus research. 2014;191:180-3. doi: 10.1016/j.virusres.2014.08.001. PubMed PMID: 25116391.
82. Moccia F, Negri S, Faris P, Perna A, De Luca A, Soda T, et al. Targeting Endolysosomal Two-Pore Channels to Treat Cardiovascular Disorders in the Novel COronaVIrus Disease 2019. Frontiers in Physiology. 2021;12(27). doi: 10.3389/fphys.2021.629119.